Title: Translation dynamics in human cells visualized at high-resolution reveal cancer drug action

Authors: Huaipeng Xing[1,2], Reiya Taniguchi[1], Iskander Khusainov[1], Jan Philipp Kreysing[1,3], Sonja Welsch[4], Beata Turoňová[1], Martin Beck[1]*

Affiliations:

[1]Department of Molecular Sociology, Max Planck Institute of Biophysics, 60438 Frankfurt am Main, Germany.

[2]Faculty of Biochemistry, Chemistry and Pharmacy, Goethe University Frankfurt am Main, 60438 Frankfurt am Main, Germany.

[3]IMPRS on Cellular Biophysics, 60438 Frankfurt am Main, Germany

[4]Central Electron Microscopy Facility, Max Planck Institute of Biophysics, 60438 Frankfurt am Main, Germany.

*Corresponding author. Email: martin.beck@biophys.mpg.de

Abstract: Ribosomes catalyze protein synthesis by cycling through various functional states. These states have been extensively characterized in vitro, yet their distribution in actively translating human cells remains elusive. Here, we used a cryo-electron tomography-based approach and resolved ribosome structures inside human cells with high resolution. These structures revealed the distribution of functional states of the elongation cycle, a Z tRNA binding site, and the dynamics of ribosome expansion segments. Ribosome structures from cells treated with Homoharringtonine, a drug used against chronic myeloid leukemia, revealed how translation dynamics were altered in situ, and resolve the small molecules within the active site of the ribosome. Thus, structural dynamics and drug effects can be assessed at high resolution within human cells.

One-Sentence Summary: Ribosome structures ranging from nanometer to near-atomic resolution within native and drug-treated human cells are revealed.

Main Text

The eukaryotic ribosome (80S) consists of two subunits (60S and 40S) that translate messenger RNA (mRNA) into proteins (*1*). Purified 80S ribosomes have been extensively studied in vitro, which has elucidated molecular details of translation (*2*, *3*). The translation process can be divided into four main stages: initiation, elongation, termination and ribosome recycling (*3*). During elongation, the rotation of the 40S, the association of elongation factors and the translocation of transfer RNAs (tRNAs) are coordinated to synthesize nascent chains (*3*). tRNAs have three canonical binding sites on the ribosome: aminoacyl (A), peptidyl (P), and exit (E) sites (*3*). A noncanonical tRNA binding site called the Z site, located in an extreme position past the E site, has been identified in structures of isolated translationally inactive mammalian ribosomes (*4*). It is speculated that the Z site may represent a late-stage intermediate of tRNA ejection downstream of the E site with similarity to internal ribosome entry site (IRES) interactions, but the exact physiological relevance remains obscure (*4*).

The 70S ribosome from *Mycoplasma pneumoniae* and 80S ribosome from *Dictyostelium discoideum* and the respective translation elongation processes have been visualized inside cells using cryo-electron tomography (cryo-ET), revealing differences in translation elongation (*5*–*7*). For example, the most abundant elongation intermediate in bacterial *M. pneumoniae* cells was the 'A, P' state, in which tRNAs were identified in the respective positions. In contrast, the elongation factor bound 'eEF1A, A/T, P' state was most abundant in eukaryotic *D. discoideum* cells. In microsomes isolated from human cells, the membrane-associated elongation cycle has been resolved, revealing the 'eEF1A, A/T, P, E' state as the most prominent (*8*). However, to which extent these insights are applicable to actively translating human cells remains unclear.

Homoharringtonine (HHT) is a natural compound that binds to the ribosome and inhibits protein synthesis (*9*). It is used to treat patients with chronic myeloid leukemia clinically and as a reference to study new anti-cancer ribosome inhibitors (*9*, *10*). The HHT-bound ribosome structure has been determined by incubating the purified 80S ribosome with HHT in vitro (*11*, *12*), revealing the binding site at the peptidyl transferase center (PTC). In the cellular context, it remains unclear how HHT affects translation dynamics and how exactly it inhibits protein synthesis. Here, we applied cryo-focused ion beam (cryo-FIB), cryo-ET and advanced data processing algorithms to determine the near-atomic structures of ribosomes and analyzed the abundance and organization of different ribosome states in untreated and HHT-treated human cells.

Ribosome is bound with HHT inside human cells

To study the 80S ribosome structures inside human cells, we first prepared cryo-FIB-milled lamellae from 35 native (untreated) human embryonic kidney (HEK) 293 cells and acquired 358 tilt-series (fig. S1A and table S1). We used template matching to identify ribosomes within the reconstructed tomograms (fig. S1B and movie S1). After classification and refinement, we determined the ribosome structure at an overall resolution of ~3.2 Å and locally resolved features up to 2.5 Å in resolution from untreated cells (Fig. 1B and figs. S1 to S3). The density of ribosomal protein side chains, ribosomal RNA (rRNA) bases, tRNA bases and ions were well resolved (fig. S1E), indicating the quality of the map. Using the same approach, we processed 352 tilt series from 32 HHT-treated cells. In the resulting structure, the density of HHT was visible (fig. S1, F and G) and the position of HHT at the PTC showed a high similarity to

previous in vitro analysis (*9*, *11*). The P-tRNA was poorly resolved compared to the untreated ribosome (fig. S1G), suggesting that the translation was altered after HHT treatment.

Translation elongation cycle in human cells

We next investigated the translation elongation process. In untreated cells, focused classification was performed with dedicated tRNA and elongation factor masks, resulting in eight ribosome states resolved from 3.4 Å to 16.4 Å (figs. S2 to S3 and table S2). These states were well-explained by previously reported structural models that captured various elongation states (figs. S4 to S6) (*4*, *8*, *13–15*). The 'eEF1A, A/T, P' state was the best resolved, globally reaching ~3.4 Å (Fig. 1A), and displayed structural features characteristic for tRNA scanning, indicating codon sampling rather than codon recognition is occurring (Fig. 1B and fig. S4A) (*13*, *16*). Specifically, the mRNA codon was more clearly resolved at the P site (Fig. 1C), suggesting that the codon-anticodon interaction at the A site is not yet established. Consistently, we observe the decoding nucleotides A1824 and A1825, which are thought to stabilize the A-site tRNA by a 'flipping out' movement upon codon recognition (*17*), in a 'flipped in' conformation (Fig. 1D).

In total, six classes accounting for ~83% of all identified ribosomes, were assigned to the translation elongation cycle based on their similarity to the previously reported structures (Fig. 2A) (*3*, *5*, *13*, *16*). The elongation cycle is thought to start from the non-unrotated 'P' state that was detected, but not particularly abundant in our data (*5*) (Fig. 2A). It is followed by the 'eEF1A, A/T, P' state discussed above that was the most prominent, consistent with in situ analysis of the lower eukaryote *Dictyostelium discoideum* (*7*), but contrasting previous analysis in bacteria (*5*). The abundance of the codon sampling state in human cells could be important for the higher decoding fidelity during translation (*18*). The following states were the non-rotated 'A/T, P' and 'A, P' states. At a low contour level of the map a factor-like density at the eEF1A binding region is seen in the 'A/T, P' state, but neither an extended nor compact eEF1A model would explain it well (fig. S4C, Materials and Methods) (*8*, *13*). As expected, the 'A, P' state displayed the A1824 and A1825 nucleotides in 'flipped out' conformation (fig. S4D). Yet it was less abundant than in bacteria, where it was the most populated (*5*). The subsequent state was identified as 'eEF2, ap/P, pe/E' (*19*). Next, two possible sequences of events are conceivable: eEF2 and E-tRNA could first dissociate from the ribosome forming the 'P' state that subsequently binds the eEF1A-tRNA, or the eEF1A-tRNA may displace eEF2 with subsequent departure of the E-tRNA (*5*) (Fig. 2A). Various conformational changes of the small subunit are apparent during the elongation cycle (fig. S5) and consistent with previous work (*16*, *19*).

Two further states were identified that are non-obvious to place in the elongation cycle (Fig. 2B). The rotated 'eEF2' state without tRNA fitted the previous structural model very well (*15*, *20*) (fig. S4G), although the eEF2 position was shifted by ~1.7 nm compared to the 'eEF2, ap/P, pe/E' state (fig. S4I). The remaining class, which accounts for only 1.6% of all classified ribosomes (Fig. 2B), was consistent with the non-rotated 'eEF1A, A/T, P, Z' state, which has been suggested to be transient (*4*). Although the resolution of this state was only moderate in untreated cells, the observed electron optical density at the Z site fitted well with the purified ribosome at the non-rotated 'P, Z' state (Fig. 2B and fig. S4, H and J) (*4*). To our knowledge, alternative factors binding to this site have not been identified. More importantly, we obtained higher resolution in HHT-treated cells (see below), which further strengthened this conclusion. We note that ~12% of the particles identified as ribosomes were not attributed to a specific state by our classification and may correspond to additional low abundant states or transitions between states. Collectively, our

data allowed the detailed analysis of the translation dynamics inside native human cells, which exhibited differences compared to previous ex vivo studies (*8*, *19*), indicating the ribosome isolation process may affect the ability to capture native elongation intermediates (*5*, *7*).

HHT alters the elongation cycle

The anti-cancer drug HHT blocks the peptide-bond formation (*9*, *21*). Previous in vitro analysis of purified ribosomes revealed that HHT binds in the A-site cleft in the PTC (*11*, *22*). Upon HHT treatment, one would thus expect to observe a strong enrichment of ribosomes with the A and P-site tRNAs bound (*11*). Indeed, *M. pneumoniae* ribosomes treated with 0.5 mg/ml (1,547.4 µM) chloramphenicol (Cm), a related antibiotic binding to the PTC of the 50S, showed over 70% of ribosomes at the 'A, P' state (*5*, *23*). The effect of HHT on human ribosome states in cells remains unknown. To address this, we exposed cells to HHT concentrations of 0.055 mg/ml (100 µM) in the medium, which resulted in a significantly lower cellular protein concentration than untreated cells (fig. S7A), implying that protein synthesis was inhibited. At the time point examined by cryo-EM, the ATP level, which serves as an indicator of cell viability, was not yet reduced (fig. S7B), and the cell morphology of untreated and treated cells was indistinguishable (fig. S7C). Classification, as described above, identified six ribosome states resolved into the 3.7 Å to 11.5 Å range (figs. S8 to S12 and table S3). Unexpectedly, the rotated state with eEF2, but without tRNA, accounted for almost half of all ribosomes in the dataset (Fig. 2, C and D, and Fig. 3A). This state showed density for SERPINE1 mRNA-binding protein 1 (SERBP1) and thus accounts for hibernating ribosomes (*15*, *24*) (fig. S10G), in which the HHT density was visible (fig. S8C). The 'P' state increased in abundance compared to the untreated cells, whereby the 'A, P' states showed a similar abundance (Fig. 2C). The HHT molecule was also resolved at the 'A, P' state, but not in other less populated classes due to the lower resolution (Fig. 3B). We therefore combined the particles from the four remaining less abundant classes. The resulting average also displayed density for HHT (fig. S8C). The positions of A-tRNA and P-tRNA at 'A, P' states were similar in untreated and HHT-treated cells (Fig. 3B) (*9*). One of our classes appeared similar to a potential 'compact eEF2, A, P' state (figs. S10, D, I and J, and S11F) (*25*), although the respective local resolution prevents a definitive assignment due to a lack of secondary structure. Finally, two states with Z-tRNA were considerably more abundant compared to untreated cells (Fig. 2D and fig. S10, C and E), showing the typical features of tRNA shape at the Z site (fig. S10, E and H, and movie S3). Thus, HHT treatment results in the accumulation of ribosome hibernation instead of the 'A, P' state, which may be representative of the mechanism of the drug action in cancer therapy.

To investigate cell-to-cell variability, we analyzed the distribution of the ribosome states across individual cells captured by multiple tomograms. We identified some degree of cell-to-cell variability (fig. S13A), for example, the 'eEF1A, A/T, P' state varied from 25% to 56% in untreated cells (fig. S13B). Overall, the signal observed in multiple tomograms of the same cell was similar, with some notable exceptions that may imply local variability (fig. S13B). Notably, the abundance of the 'eEF1A, A/T, P' (class 1) and 'eEF1A, A/T, P, E' (class 4) was largely anticorrelated in untreated cells (fig. S13, C and D), while the sum of eEF1A-bound states was relatively consistent, suggesting that its total concentration may be limited (fig. S13E). In contrast, the abundance of ribosomes containing eEF2 was much more diverse between different cells (fig. S13E).

Polysomes are impaired upon the HHT treatment

We analyzed the spatial organization of different ribosome states within polysomes in treated and untreated cells. The densities accounting for neighboring ribosomes that are commonly observed in the subtomogram averages of untreated cells were reduced in HHT-treated cells (fig. S14A). Furthermore, the ribosome distribution was more dispersed subsequent to treatment (Fig. 4, A and B), both implying that polysomes might be largely abolished. To test this hypothesis, we defined polysomes based on a distance threshold of 9 nm from the mRNA exit to entry sites of neighboring particles in this study (fig. S14B and table S4, Materials and methods). While this arbitrary classifier will not capture the entirety of polyribosomes, as it could for example miss more distantly spaced ribosomes on a longer transcript, it overall performs well in their detection. 30.2% of all ribosomes in untreated cells were grouped into arbitrary polysomes (Fig. 4C and fig. S14, C and D), which was considerably higher than in HHT-treated cells (fig. S15, A to E). In monosomes the 'eEF2' state was prevalent (Fig. 4D and fig. S16, A and B) and exhibits much less neighboring density (fig. S16, C and D), underlining the notion that these ribosomes are hibernating. In polysomes, the 'eEF2, ap/P, pe/E' state (class 3, see Fig 3A) was less frequent in the first leading ribosome than the trailing ribosomes (fig. S15F). Classification of all untreated ribosomes with a dedicated mask resolved the low-resolution structure of the di-ribosome, in which the mRNA density was visible (fig. S17A) (*26*, *27*). This di-ribosome resembled the 'top-to-top' configuration (t-t, the central protuberance of both ribosomes facing a similar direction) (*28*, *29*) (fig. S17B). Two other arrangements of pairs were apparent: one with the central protuberance of the 'i+1' ribosome towards down (t-d), the other towards up (t-u) (fig. S17, C and D). Although the abundance of these configurations declined in the treated cells (fig. S17, D and E), the center-to-center and exit-to-entry distance of these pairs were indistinguishable from untreated cells (fig. S17F).

We classified ribosomes with a mask covering the region beyond the exit tunnel, thus capturing both the potential membrane and the expansion segment ES27L (figs. S18 and S19, and tables S2 and S3). The analysis revealed that the translation state distributions of soluble and membrane-bound ribosomes were similar (fig. S18D). Notably, seven conformations of the expansion segment ES27L were found in cytosolic ribosomes (fig. S19, Materials and methods). One of these contains a long stretch of ES27L that associates with the ErbB3 receptor-binding protein (Ebp1) on the surface of the 60S and resembles a previously published in vitro structure (*30*, *31*) (fig. S19, A and B, tables S2 and S3). The percentage of Ebp1-associated ribosomes was below 20% in most untreated cells, while the abundance was over 25% in all HHT-treated cells (fig. S20A). Whether Ebp1 is related to specific translation states remained unclear (*30*, *31*). Thus, a subfraction of Ebp1-bound ribosomes is observed in all apparent intermediates of the elongation cycle (fig. S20B).

HHT binds the free 60S associated with eIF6

Finally, we investigated the free 60S and 40S in the cytoplasm of human cells. The free 60S showed Ebp1 and ES27L density in both datasets (Fig. 5, A and B, fig. S21, A and B), which was similar to the Ebp1-associated 80S ribosome. However, the 60S was much more abundant in treated cells than in untreated cells (Fig. 5C). Eukaryotic initiation factor 6 (eIF6) binds the 60S to prevent premature 60S binding with 40S (*32*, *33*). Our data show that the 60S did not contain eIF6 in the cytosol of native untreated cells, contrasting HHT-treated cells (Fig. 5D). Thus, it appears that eIF6 prevents the association between large and small ribosomal subunits in cells (*34*–*36*) (Fig. 5, C and D, and fig. S21, C to E). Furthermore, the HHT density was resolved in the

60S from treated cells (Fig. 5E). Thus, we conclude that HHT can bind not only the PTC of different states of 80S ribosome (Fig. 3B and fig. S8C), but also the free 60S decorated with eIF6, which may block the assembly of 40S and 60S in the cytosol of the cell.

Discussion

Our extensive cryo-ET analysis stresses the feasibility of obtaining structures at high resolution and visualizes an anti-cancer drug inside human cells. The local resolution in the ribosome core in our study is limited by the pixel size. This illustrates that technical obstacles that hinder high resolution in cellular tomography have been overcome. The combined improvements in energy filtering (*37*), image processing (Warp-RELION-M pipeline) (*23*), and tight control over specimen thickness (*38*, *39*) enable high resolution, as long as the number of particles that can be obtained is sufficient. Further improvements in the automatization of specimen preparation techniques may thus be instrumental in pushing the resolution for other macromolecular assemblies analyzed inside cells (*39–44*).

The detailed comparison of ribosome structures within untreated and HHT-treated cells revealed that HHT bound to the PTC of the 80S ribosome in situ (Fig. 3B and figs. S1G and S8C), where it can block peptide bond formation as suggested by previous in vitro studies (*9*, *11*, *22*). However, we also observe SERBP1 binding to ribosomes, a factor that functions downstream of mammalian target of rapamycin complex 1 (mTORC1) and leads to a dormant ribosome state (*45*). Such ribosome hibernation can be a result of cellular stress signalling (*45*). Further, we uncovered that HHT bound the free 60S associated with eIF6 (Fig. 5, D and E), thus likely hampering the assembly of functional 80S ribosomes, and in turn further impairing overall protein synthesis. The accumulation of 60S-eIF6 may be explained by the fact that the HHT biding site overlaps with that of the N-terminus of Shwachman-Bodian-Diamond syndrome protein (SBDS) (fig. S21F), and the binding of SBDS to 60S is necessary to release eIF6 (*35*, *46*).

Our study provides insights into the translation elongation cycle, the coordination of ribosome activity within polysomes and the diverse arrangements of ES27L inside human cells. One may use the same technology in the future to investigate ribosome, translation and mRNA quality control pathways in the context of human tissue culture cells and primary patient derived cells. Intermediates that have not yet been observed inside cells may be enriched by introducing kinetical bottlenecks, through genetic or pharmaceutical perturbation (*5*, *47*, *48*). Our study may set the stage for the analysis of structures inside mammalian cells and characterizing drug susceptibility of human individuals at high resolution by cryo-ET.

References and Notes

1. V. Ramakrishnan, The Ribosome Emerges from a Black Box. *Cell*. **159**, 979–984 (2014).
2. A. A. Korostelev, The Structural Dynamics of Translation. *https://doi.org/10.1146/annurev-biochem-071921-122857*. **91**, 245–267 (2022).
3. A. P. Schuller, R. Green, Roadblocks and resolutions in eukaryotic translation. *Nature Reviews Molecular Cell Biology 2018 19:8*. **19**, 526–541 (2018).
4. A. Brown, M. R. Baird, M. C. J. Yip, J. Murray, S. Shao, Structures of translationally inactive mammalian ribosomes. *Elife*. **7** (2018), doi:10.7554/ELIFE.40486.
5. L. Xue, S. Lenz, M. Zimmermann-Kogadeeva, D. Tegunov, P. Cramer, P. Bork, J. Rappsilber, J. Mahamid, Visualizing translation dynamics at atomic detail inside a bacterial cell. *Nature 2022 610:7930*. **610**, 205–211 (2022).

6. F. J. O'Reilly, L. Xue, A. Graziadei, L. Sinn, S. Lenz, D. Tegunov, C. Blötz, N. Singh, W. J. H. Hagen, P. Cramer, J. Stülke, J. Mahamid, J. Rappsilber, In-cell architecture of an actively transcribing-translating expressome. *Science*. **369**, 554 (2020).
7. P. C. Hoffmann, J. P. Kreysing, I. Khusainov, M. W. Tuijtel, S. Welsch, M. Beck, Structures of the eukaryotic ribosome and its translational states in situ. *Nature Communications 2022 13:1*. **13**, 1–9 (2022).
8. M. Gemmer, M. L. Chaillet, J. van Loenhout, R. Cuevas Arenas, D. Vismpas, M. Gröllers-Mulderij, F. A. Koh, P. Albanese, R. A. Scheltema, S. C. Howes, A. Kotecha, J. Fedry, F. Förster, Visualization of translation and protein biogenesis at the ER membrane. *Nature 2023*, 1–8 (2023).
9. A. Gilles, L. Frechin, K. Natchiar, G. Biondani, O. von Loeffelholz, S. Holvec, J. L. Malaval, J. Y. Winum, B. P. Klaholz, J. F. Peyron, Targeting the Human 80S Ribosome in Cancer: From Structure to Function and Drug Design for Innovative Adjuvant Therapeutic Strategies. *Cells*. **9** (2020), doi:10.3390/CELLS9030629.
10. V. Kumar, Jyotirmayee, M. Verma, Developing therapeutic approaches for chronic myeloid leukemia: a review. *Molecular and Cellular Biochemistry 2022*. **1**, 1–17 (2022).
11. N. Garreau De Loubresse, I. Prokhorova, W. Holtkamp, M. v. Rodnina, G. Yusupova, M. Yusupov, Structural basis for the inhibition of the eukaryotic ribosome. *Nature 2014 513:7519*. **513**, 517–522 (2014).
12. S. K. Natchiar, A. G. Myasnikov, H. Kratzat, I. Hazemann, B. P. Klaholz, Visualization of chemical modifications in the human 80S ribosome structure. *Nature 2017 551:7681*. **551**, 472–477 (2017).
13. S. Shao, J. Murray, A. Brown, J. Taunton, V. Ramakrishnan, R. S. Hegde, Decoding Mammalian Ribosome-mRNA States by Translational GTPase Complexes. *Cell*. **167**, 1229-1240.e15 (2016).
14. R. Buschauer, Y. Matsuo, T. Sugiyama, Y. H. Chen, N. Alhusaini, T. Sweet, K. Ikeuchi, J. Cheng, Y. Matsuki, R. Nobuta, A. Gilmozzi, O. Berninghausen, P. Tesina, T. Becker, J. Coller, T. Inada, R. Beckmann, The Ccr4-Not complex monitors the translating ribosome for codon optimality. *Science (1979)*. **368** (2020), doi:10.1126/SCIENCE.AAY6912/SUPPL_FILE/AAY6912_S1.MP4.
15. J. N. Wells, R. Buschauer, T. Mackens-Kiani, K. Best, H. Kratzat, O. Berninghausen, T. Becker, W. Gilbert, J. Cheng, R. Beckmann, Structure and function of yeast Lso2 and human CCDC124 bound to hibernating ribosomes. *PLoS Biol*. **18**, e3000780 (2020).
16. T. V. Budkevich, J. Giesebrecht, E. Behrmann, J. Loerke, D. J. F. Ramrath, T. Mielke, J. Ismer, P. W. Hildebrand, C. S. Tung, K. H. Nierhaus, K. Y. Sanbonmatsu, C. M. T. Spahn, Regulation of the Mammalian Elongation Cycle by Subunit Rolling: A Eukaryotic-Specific Ribosome Rearrangement. *Cell*. **158**, 121–131 (2014).
17. S. Shao, J. Murray, A. Brown, J. Taunton, V. Ramakrishnan, R. S. Hegde, Decoding Mammalian Ribosome-mRNA States by Translational GTPase Complexes. *Cell*. **167**, 1229-1240.e15 (2016).
18. A. Rozov, N. Demeshkina, E. Westhof, M. Yusupov, G. Yusupova, New Structural Insights into Translational Miscoding. *Trends Biochem Sci*. **41**, 798–814 (2016).
19. E. Behrmann, J. Loerke, T. V. Budkevich, K. Yamamoto, A. Schmidt, P. A. Penczek, M. R. Vos, J. Bürger, T. Mielke, P. Scheerer, C. M. T. Spahn, Structural Snapshots of Actively Translating Human Ribosomes. *Cell*. **161**, 845–857 (2015).
20. P. R. Smith, S. Loerch, N. Kunder, A. D. Stanowick, T. F. Lou, Z. T. Campbell, Functionally distinct roles for eEF2K in the control of ribosome availability and p-body abundance. *Nature Communications 2021 12:1*. **12**, 1–16 (2021).
21. S. Pellegrino, S. Terrosu, G. Yusupova, M. Yusupov, Inhibition of the eukaryotic 80S ribosome as a potential anticancer therapy: A structural perspective. *Cancers (Basel)*. **13** (2021), doi:10.3390/CANCERS13174392/S1.
22. G. Gürel, G. Blaha, P. B. Moore, T. A. Steitz, U2504 Determines the Species Specificity of the A-Site Cleft Antibiotics:: The Structures of Tiamulin, Homoharringtonine, and Bruceantin Bound to the Ribosome. *J Mol Biol*. **389**, 146–156 (2009).
23. D. Tegunov, L. Xue, C. Dienemann, P. Cramer, J. Mahamid, Multi-particle cryo-EM refinement with M visualizes ribosome-antibiotic complex at 3.5 Å in cells. *Nature Methods 2021 18:2*. **18**, 186–193 (2021).
24. P. R. Smith, S. C. Pandit, S. Loerch, Z. T. Campbell, The space between notes: emerging roles for translationally silent ribosomes. *Trends Biochem Sci*. **47** (2022), , doi:10.1016/j.tibs.2022.02.003.
25. J. Lin, M. G. Gagnon, D. Bulkley, T. A. Steitz, Conformational Changes of Elongation Factor G on the Ribosome during tRNA Translocation. *Cell*. **160**, 219–227 (2015).
26. K. Ikeuchi, P. Tesina, Y. Matsuo, T. Sugiyama, J. Cheng, Y. Saeki, K. Tanaka, T. Becker, R. Beckmann, T. Inada, Collided ribosomes form a unique structural interface to induce Hel2-driven quality control pathways. *EMBO J*. **38**, e100276 (2019).
27. M. Narita, T. Denk, Y. Matsuo, T. Sugiyama, C. Kikuguchi, S. Ito, N. Sato, T. Suzuki, S. Hashimoto, I. Machová, P. Tesina, R. Beckmann, T. Inada, A distinct mammalian disome collision interface harbors K63-

linked polyubiquitination of uS10 to trigger hRQT-mediated subunit dissociation. *Nature Communications 2022 13:1*. **13**, 1–16 (2022).
28. F. Brandt, S. A. Etchells, J. O. Ortiz, A. H. Elcock, F. U. Hartl, W. Baumeister, The Native 3D Organization of Bacterial Polysomes. *Cell*. **136**, 261–271 (2009).
29. F. Brandt, L. A. Carlson, F. U. Hartl, W. Baumeister, K. Grünewald, The Three-Dimensional Organization of Polyribosomes in Intact Human Cells. *Mol Cell*. **39**, 560–569 (2010).
30. K. Wild, M. Aleksić, K. Lapouge, K. D. Juaire, D. Flemming, S. Pfeffer, I. Sinning, MetAP-like Ebp1 occupies the human ribosomal tunnel exit and recruits flexible rRNA expansion segments. *Nature Communications 2020 11:1*. **11**, 1–10 (2020).
31. M. L. Kraushar, F. Krupp, D. Harnett, P. Turko, M. C. Ambrozkiewicz, T. Sprink, K. Imami, M. Günnigmann, U. Zinnall, C. H. Vieira-Vieira, T. Schaub, A. Münster-Wandowski, J. Bürger, E. Borisova, H. Yamamoto, M. R. Rasin, U. Ohler, D. Beule, T. Mielke, V. Tarabykin, M. Landthaler, G. Kramer, I. Vida, M. Selbach, C. M. T. Spahn, Protein Synthesis in the Developing Neocortex at Near-Atomic Resolution Reveals Ebp1-Mediated Neuronal Proteostasis at the 60S Tunnel Exit. *Mol Cell*. **81**, 304-322.e16 (2021).
32. D. W. Russell, L. L. Spremulli, Purification and characterization of a ribosome dissociation factor (eukaryotic initiation factor 6) from wheat germ. *Journal of Biological Chemistry*. **254**, 8796–8800 (1979).
33. M. Gartmann, M. Blau, J. P. Armache, T. Mielke, M. Topf, R. Beckmann, Mechanism of eIF6-mediated Inhibition of Ribosomal Subunit Joining. *Journal of Biological Chemistry*. **285**, 14848–14851 (2010).
34. M. Ceci, C. Gaviraghi, C. Gorrini, L. A. Sala, N. Offenhäuser, P. C. Marchisio, S. Biffo, Release of eIF6 (p27BBP) from the 60S subunit allows 80S ribosome assembly. *Nature 2004 426:6966*. **426**, 579–584 (2003).
35. F. Weis, E. Giudice, M. Churcher, L. Jin, C. Hilcenko, C. C. Wong, D. Traynor, R. R. Kay, A. J. Warren, Mechanism of eIF6 release from the nascent 60S ribosomal subunit. *Nature Structural & Molecular Biology 2015 22:11*. **22**, 914–919 (2015).
36. P. Jaako, A. Faille, S. Tan, C. C. Wong, N. Escudero-Urquijo, P. Castro-Hartmann, P. Wright, C. Hilcenko, D. J. Adams, A. J. Warren, eIF6 rebinding dynamically couples ribosome maturation and translation. *Nature Communications 2022 13:1*. **13**, 1–11 (2022).
37. M. Obr, W. J. H. Hagen, R. A. Dick, L. Yu, A. Kotecha, F. K. M. Schur, Exploring high-resolution cryo-ET and subtomogram averaging capabilities of contemporary DEDs. *J Struct Biol*. **214**, 107852 (2022).
38. A. Rigort, J. M. Plitzko, Cryo-focused-ion-beam applications in structural biology. *Arch Biochem Biophys*. **581**, 122–130 (2015).
39. S. Klumpe, H. K. H. Fung, S. K. Goetz, I. Zagoriy, B. Hampoelz, X. Zhang, P. S. Erdmann, J. Baumbach, C. W. Müller, M. Beck, J. M. Plitzko, J. Mahamid, A modular platform for automated cryo-FIB workflows. *Elife*. **10** (2021), doi:10.7554/ELIFE.70506.
40. M. Smeets, A. Bieber, C. Capitanio, O. Schioetz, T. van der Heijden, A. Effting, É. Piel, B. Lazem, P. Erdmann, J. Plitzko, Integrated Cryo-Correlative Microscopy for Targeted Structural Investigation In Situ. *Micros Today*. **29**, 20–25 (2021).
41. S. Klumpe, J. Kuba, O. H. Schioetz, P. S. Erdmann, A. Rigort, J. M. Plitzko, Recent Advances in Gas Injection System-Free Cryo-FIB Lift-Out Transfer for Cryo-Electron Tomography of Multicellular Organisms and Tissues. *Micros Today*. **30**, 42–47 (2022).
42. Z. Wang, M. Grange, S. Pospich, T. Wagner, A. L. Kho, M. Gautel, S. Raunser, Structures from intact myofibrils reveal mechanism of thin filament regulation through nebulin. *Science (1979)*. **375** (2022), doi:10.1126/SCIENCE.ABN1934/SUPPL_FILE/SCIENCE.ABN1934_MOVIES_S1_TO_S4.ZIP.
43. H. van den Hoek, N. Klena, M. A. Jordan, G. A. Viar, R. D. Righetto, M. Schaffer, P. S. Erdmann, W. Wan, S. Geimer, J. M. Plitzko, W. Baumeister, G. Pigino, V. Hamel, P. Guichard, B. D. Engel, In situ architecture of the ciliary base reveals the stepwise assembly of intraflagellar transport trains. *Science (1979)*. **377**, 543–548 (2022).
44. S. Mosalaganti, A. Obarska-Kosinska, M. Siggel, R. Taniguchi, B. Turoňová, C. E. Zimmerli, K. Buczak, F. H. Schmidt, E. Margiotta, M. T. Mackmull, W. J. H. Hagen, G. Hummer, J. Kosinski, M. Beck, AI-based structure prediction empowers integrative structural analysis of human nuclear pores. *Science (1979)*. **376** (2022), doi:10.1126/SCIENCE.ABM9506/SUPPL_FILE/SCIENCE.ABM9506_MDAR_REPRODUCIBILITY_CHECKLIST.PDF.
45. S. Shetty, J. Hofstetter, S. Battaglioni, D. Ritz, M. N. Hall, TORC1 phosphorylates and inhibits the ribosome preservation factor Stm1 to activate dormant ribosomes. *EMBO J*. **42**, e112344 (2023).

46. P. Jaako, A. Faille, S. Tan, C. C. Wong, N. Escudero-Urquijo, P. Castro-Hartmann, P. Wright, C. Hilcenko, D. J. Adams, A. J. Warren, eIF6 rebinding dynamically couples ribosome maturation and translation. *Nature Communications 2022 13:1*. **13**, 1–11 (2022).
47. M. Thoms, R. Buschauer, M. Ameismeier, L. Koepke, T. Denk, M. Hirschenberger, H. Kratzat, M. Hayn, T. MacKens-Kiani, J. Cheng, J. H. Straub, C. M. Stürzel, T. Fröhlich, O. Berninghausen, T. Becker, F. Kirchhoff, K. M. J. Sparrer, R. Beckmann, Structural basis for translational shutdown and immune evasion by the Nsp1 protein of SARS-CoV-2. *Science (1979)*. **369**, 1249–1256 (2020).
48. S. Klinge, J. L. Woolford, Ribosome assembly coming into focus. *Nature Reviews Molecular Cell Biology 2018 20:2*. **20**, 116–131 (2018).
49. M. Allegretti, C. E. Zimmerli, V. Rantos, F. Wilfling, P. Ronchi, H. K. H. Fung, C. W. Lee, W. Hagen, B. Turoňová, K. Karius, M. Börmel, X. Zhang, C. W. Müller, Y. Schwab, J. Mahamid, B. Pfander, J. Kosinski, M. Beck, In-cell architecture of the nuclear pore and snapshots of its turnover. *Nature 2020 586:7831*. **586**, 796–800 (2020).
50. Y. Chen, T. B. Lear, J. W. Evankovich, M. B. Larsen, B. Lin, I. Alfaras, J. R. Kennerdell, L. Salminen, D. P. Camarco, K. C. Lockwood, F. Tuncer, J. Liu, M. M. Myerburg, J. F. McDyer, Y. Liu, T. Finkel, B. B. Chen, A high-throughput screen for TMPRSS2 expression identifies FDA-approved compounds that can limit SARS-CoV-2 entry. *Nature Communications 2021 12:1*. **12**, 1–15 (2021).
51. P. Li, Y. Li, Y. Wang, J. Liu, M. Lavrijsen, Y. Li, R. Zhang, M. M. A. Verstegen, Y. Wang, T. C. Li, Z. Ma, D. E. Kainov, M. J. Bruno, R. A. de Man, L. J. W. van der Laan, M. P. Peppelenbosch, Q. Pan, Recapitulating hepatitis E virus-host interactions and facilitating antiviral drug discovery in human liver-derived organoids. *Sci Adv*. **8** (2022), doi:10.1126/SCIADV.ABJ5908/SUPPL_FILE/SCIADV.ABJ5908_SM.PDF.
52. K. T. Choy, A. Y. L. Wong, P. Kaewpreedee, S. F. Sia, D. Chen, K. P. Y. Hui, D. K. W. Chu, M. C. W. Chan, P. P. H. Cheung, X. Huang, M. Peiris, H. L. Yen, Remdesivir, lopinavir, emetine, and homoharringtonine inhibit SARS-CoV-2 replication in vitro. *Antiviral Res*. **178**, 104786 (2020).
53. A. G. Myasnikov, S. Kundhavai Natchiar, M. Nebout, I. Hazemann, V. Imbert, H. Khatter, J. F. Peyron, B. P. Klaholz, Structure–function insights reveal the human ribosome as a cancer target for antibiotics. *Nature Communications 2016 7:1*. **7**, 1–8 (2016).
54. M. Zhang, D. Aguilera, C. Das, H. Vasquez, P. Zage, V. Gopalakrishnan, J. Wolff, Measuring Cytotoxicity: A New Perspective on LC50. *Anticancer Res*. **27**, 35–38 (2007).
55. D. N. Mastronarde, Automated electron microscope tomography using robust prediction of specimen movements. *J Struct Biol*. **152**, 36–51 (2005).
56. A. Iudin, P. K. Korir, S. Somasundharam, S. Weyand, C. Cattavitello, N. Fonseca, O. Salih, G. J. Kleywegt, A. Patwardhan, EMPIAR: the Electron Microscopy Public Image Archive. *Nucleic Acids Res*. **51**, D1503–D1511 (2023).
57. D. N. Mastronarde, Dual-Axis Tomography: An Approach with Alignment Methods That Preserve Resolution. *J Struct Biol*. **120**, 343–352 (1997).
58. D. N. Mastronarde, S. R. Held, Automated tilt series alignment and tomographic reconstruction in IMOD. *J Struct Biol*. **197**, 102–113 (2017).
59. W. Wan, williamnwan/STOPGAP: STOPGAP 0.7.1 (2020), doi:10.5281/ZENODO.3973664.
60. N. Sofroniew, T. Lambert, K. Evans, J. Nunez-Iglesias, G. Bokota, P. Winston, G. Peña-Castellanos, K. Yamauchi, M. Bussonnier, D. Doncila Pop, A. Can Solak, Z. Liu, P. Wadhwa, A. Burt, G. Buckley, A. Sweet, L. Migas, V. Hilsenstein, L. Gaifas, J. Bragantini, J. Rodríguez-Guerra, H. Muñoz, J. Freeman, P. Boone, A. Lowe, C. Gohlke, L. Royer, A. PIERRÉ, H. Har-Gil, A. McGovern, napari: a multi-dimensional image viewer for Python (2022), doi:10.5281/ZENODO.7276432.
61. T. A. M. Bharat, S. H. W. Scheres, Resolving macromolecular structures from electron cryo-tomography data using subtomogram averaging in RELION. *Nature Protocols 2016 11:11*. **11**, 2054–2065 (2016).
62. T. D. Goddard, C. C. Huang, E. C. Meng, E. F. Pettersen, G. S. Couch, J. H. Morris, T. E. Ferrin, UCSF ChimeraX: Meeting modern challenges in visualization and analysis. *Protein Sci*. **27**, 14 (2018).
63. U. H. Ermel, S. M. Arghittu, A. S. Frangakis, ArtiaX: An Electron Tomography Toolbox for the Interactive Handling of Sub-Tomograms in UCSF ChimeraX. *Protein Science*, e4472 (2022).
64. F. Brandt, L. A. Carlson, F. U. Hartl, W. Baumeister, K. Grünewald, The Three-Dimensional Organization of Polyribosomes in Intact Human Cells. *Mol Cell*. **39**, 560–569 (2010).
65. D. Q. Huynh, Metrics for 3D rotations: Comparison and analysis. *J Math Imaging Vis*. **35**, 155–164 (2009).

Acknowledgments: We thank Patrick C. Hoffmann, Maarten Tuijtel and Tomas Majtner from the Department for Molecular Sociology at the Max Planck Institute of Biophysics for advice on membrane segmentation, data collection and data processing. We thank all the members from the Central Electron Microscopy facility and the Department for Molecular Sociology at the Max Planck Institute of Biophysics, Andre Schwarz, Erin Schuman and the Department of Synaptic Plasticity at the Max Planck Institute of Brain Research for support and advice. We acknowledge the support from the Max Planck Computing and Data Facility. We thank Marina Rodnina, Niels Fischer and Stefanie Böehm for critical reading of the manuscript.

Funding: M.B. acknowledges funding from the Max Planck Society.

Author contributions: Conceptualization: H.X., M.B.; Methodology: H.X., B.T., I.K., J.P.K.; Investigation: H.X., R.T., I.K., J.P.K., S.W., B.T.; Visualization: H.X., B.T., M.B.; Funding acquisition: M.B.; Project administration: H.X., M.B.; Supervision: H.X., M.B.; Writing – original draft: H.X., B.T., M.B.; Writing – review & editing: H.X., R.T., I.K., J.P.K., S.W., B.T., M.B.

Competing interests: The authors declare no competing interests.

Data and materials availability: The original tilt series have been deposited in the Electron Microscopy Public Image Archive (EMPIAR-11538). EM maps have been deposited in the Electron Microscopy Data Bank (EMDB) under accession numbers: EMD-16721, 16725, 16726, 16727, 16728, 16733, 16734, 16735, 16736, 16737, 16738, 16739, 16740, 16741, 16742, 16743, 16722, 16744, 16748, 16747, 16749, 16750, 16751, 16752, 16754, 16755, 16756, 16757. All these maps will be released upon publication and are available for the review process using the following link:
https://oc.biophys.mpg.de/owncloud/s/ZTsiCWxeHq42FP6

Password: humanribosome

The code for polysome tracing and analysis will be publicly available on GitHub upon publication and is available upon request during the review process.

Supplementary Materials

Materials and Methods

Figs. S1 to S21

Tables S1 to S4

References (*49–65*)

Movies S1 to S3

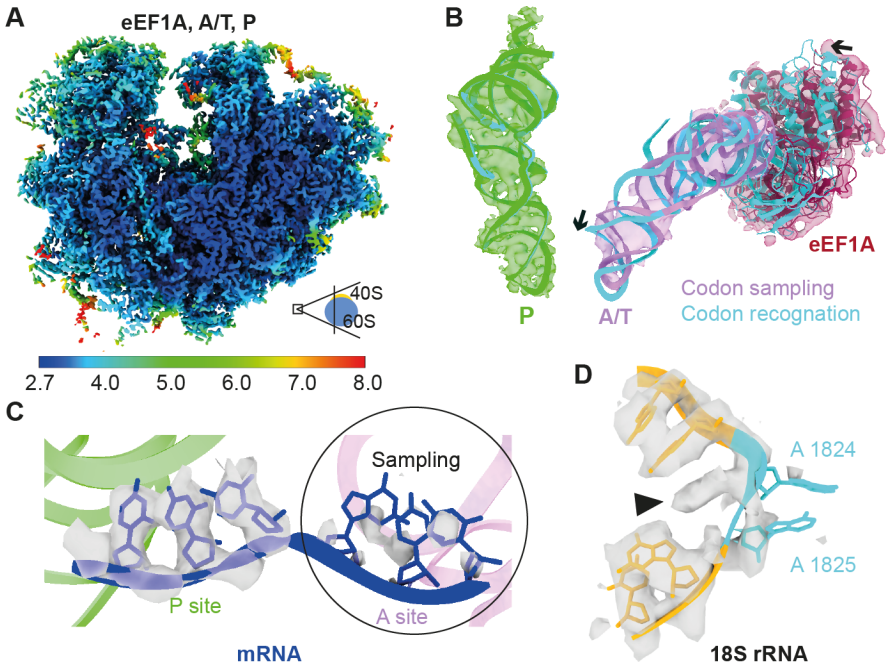

Fig. 1. 80S ribosome structures in human cells.
(**A**) Color-coded local resolution map of the 'eEF1A, A/T, P' state identified in the untreated dataset. (**B**) Superposition of the codon recognition state (PDB 5LZS, cyan) onto our eEF1A-tRNA ternary complex at the 'eEF1A, A/T, P' state. The atomic model of tRNA (lavender) and eEF1A (maroon) from PDB 4CXG were fitted into our map for comparison to 5LZS. (**C**) The mRNA segmented from the 'eEF1A, A/T, P' state was fitted with PDB 5LZS. Density is more clearly defined at the P site as compared to the A site. (**D**) The atomic model (5LZS) of 18S rRNA (A1822 to A1827) was rigid-body-fitted into the corresponding density of the 80S at the 'eEF1A, A/T, P' state. The decoding nucleotides A1824 and A1825 in the atomic model are in the flipped-out configuration, which is inconsistent with the observed density (arrowhead).

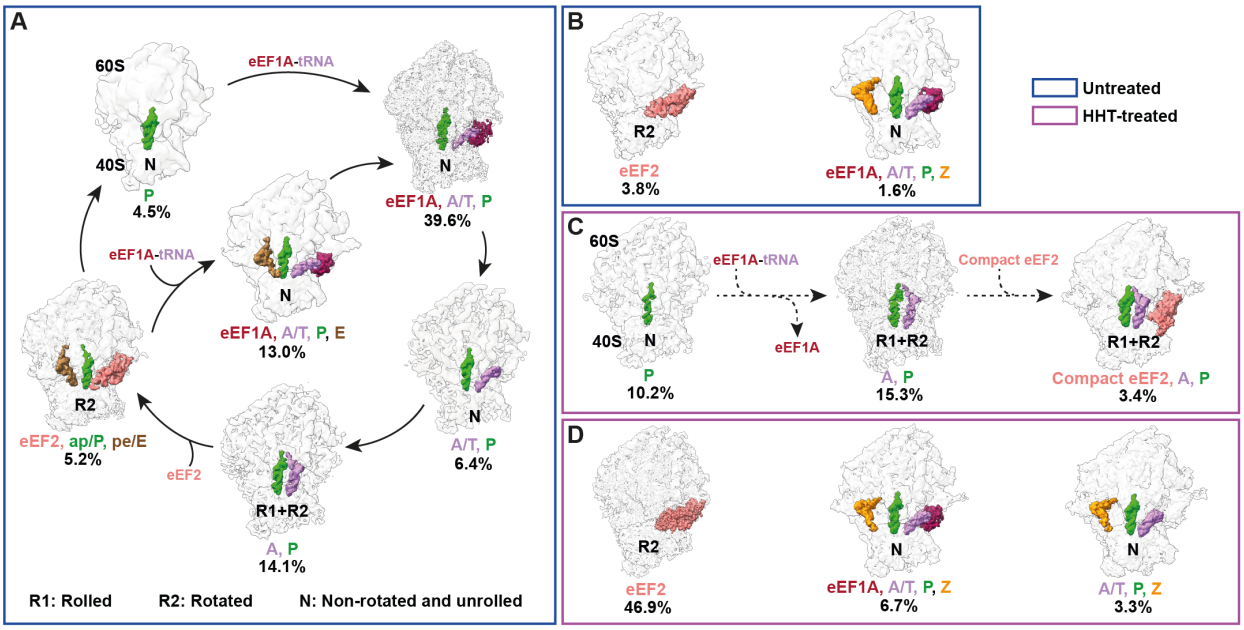

Fig. 2. Ribosome states in native untreated and HHT-treated cells.
(**A**) Six ribosome states are assigned to the elongation cycle in untreated cells. (**B**) The 'eEF2' and 'eEF1A, A/T, P, Z' states in untreated cells. (**C**) Three potential translation elongation intermediate states in the HHT-treated cells. The dashed arrow illustrates how the elongation states may connect. (**D**) The 'eEF2', 'eEF1A, A/T, P, Z' and 'A/T, P, Z' states inside the treated cells. R1, Rolled. R2, Rotated. N, Non-rotated and unrolled. The information about 40S rolling and rotation is shown in figs. S5 and S11.

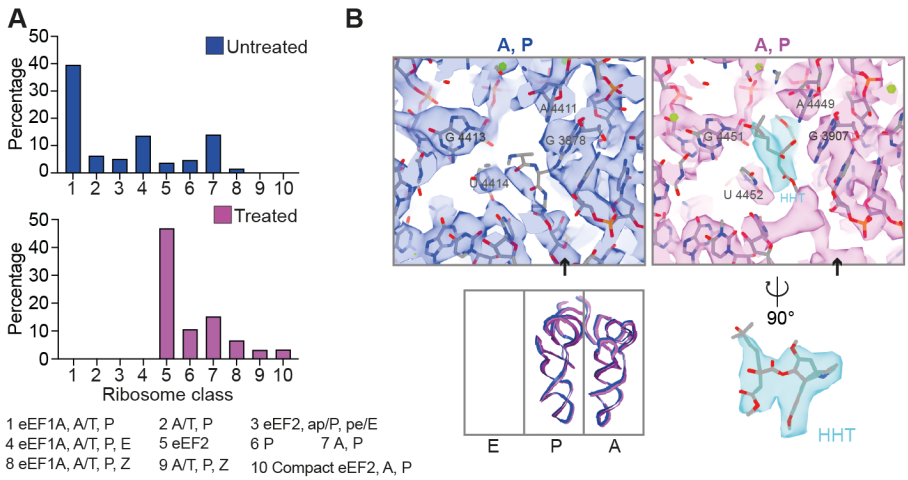

Fig. 3. Distribution of ribosome states in cells.

(**A**) Percentages of ribosome states in untreated and HHT-treated cells. (**B**) The PTC of ribosomes at the 'A, P' state in untreated and treated cells is shown fitted with PDBs 5AJ0 and 6QZP, respectively. Structural overlay of tRNAs at 'A, P' states with models determined from previous studies (bottom, Materials and methods). The black arrow points to P-tRNA. HHT is colored in cyan.

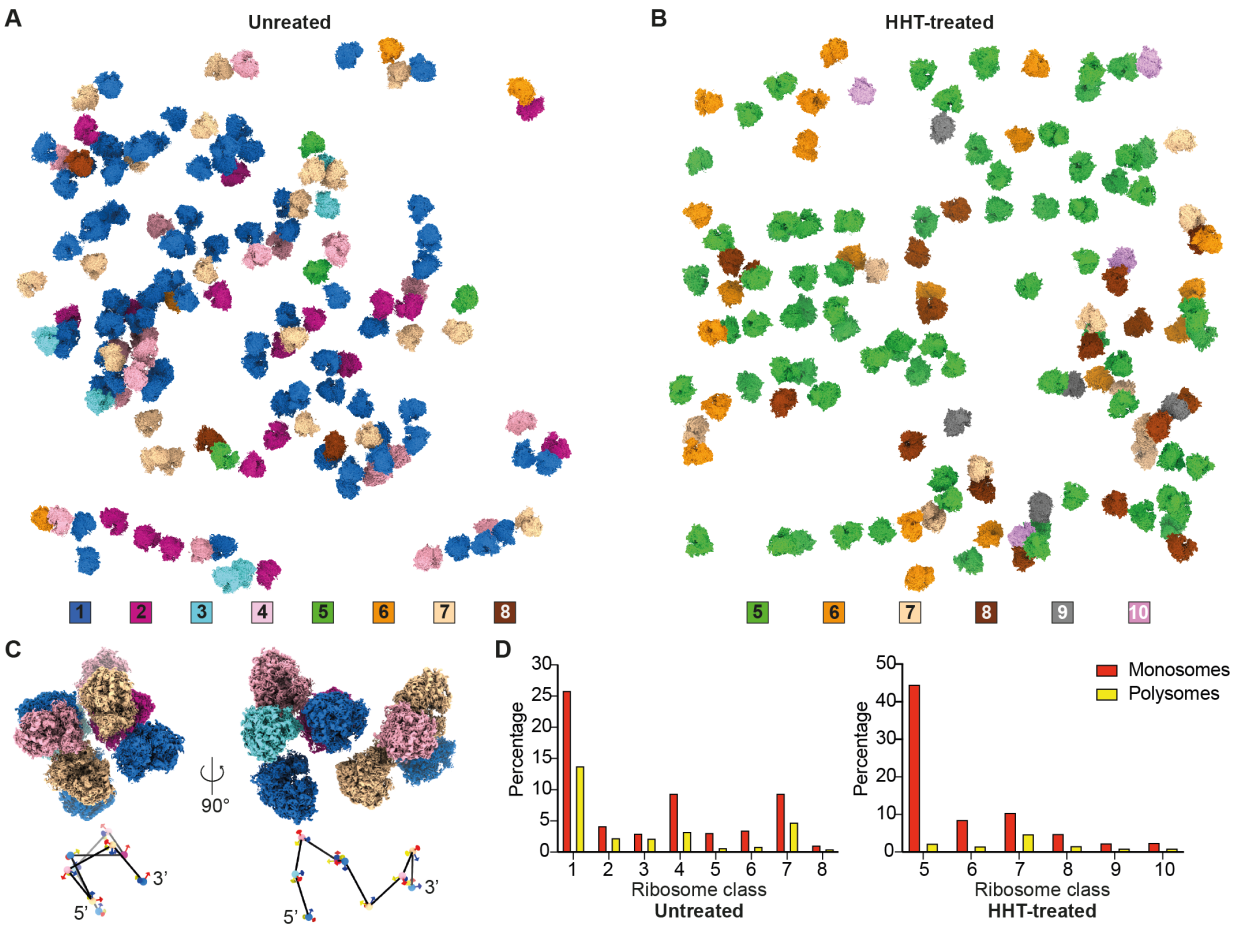

Fig. 4. Spatial and functional analysis of Polysomes.
(**A and B**) Distribution of ribosome states in a representative tomogram from an untreated (A) and treated cell (B). (**C**) A polysome and the putative mRNA path. The center-to-center distance of the neighboring ribosomes: 27.3 ± 1.8 nm (mean ± SD, n=8). (**D**) Distribution of ribosome states in monosomes and polysomes from 358 tomograms of untreated cells and 352 tomograms of treated cells. Class numbers are the same as in Fig. 3A.

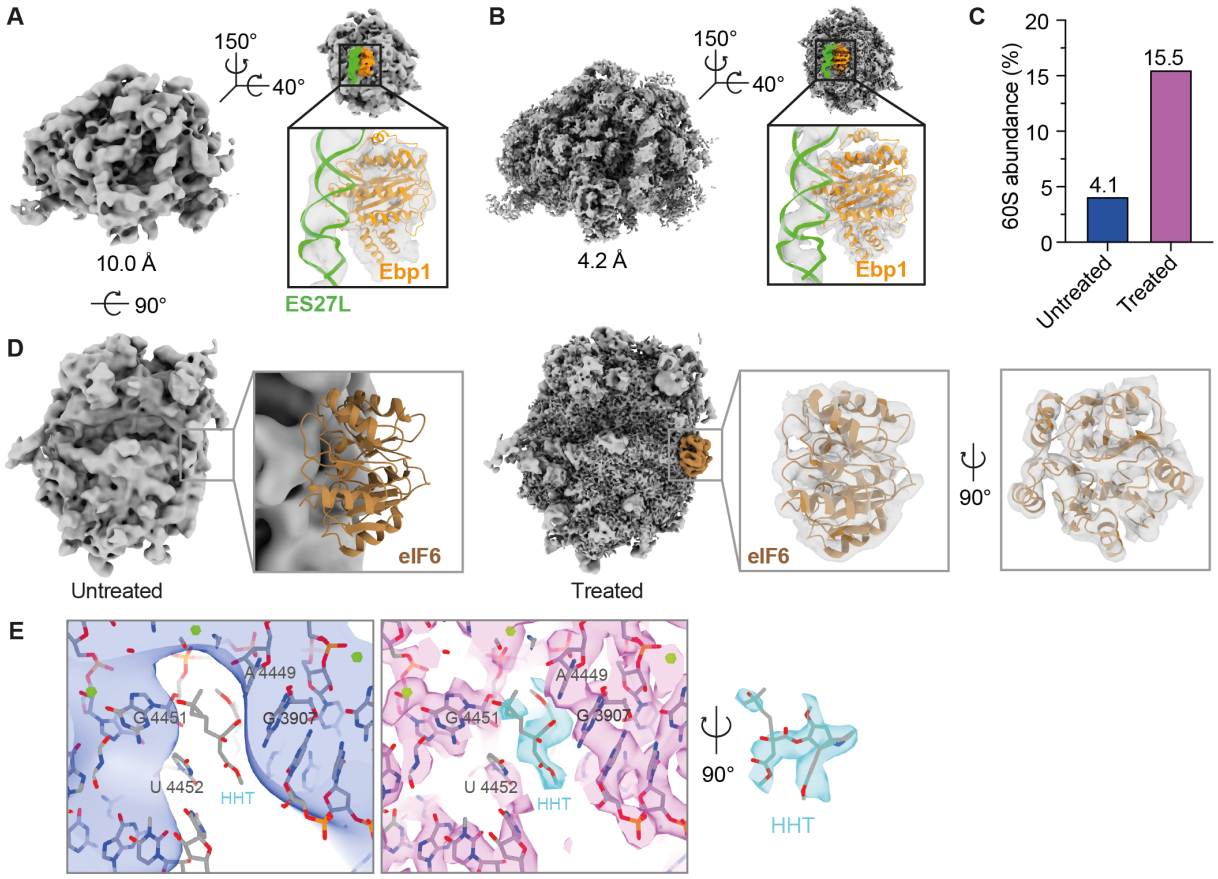

Fig. 5. Structure of 60S in human cells.

(**A** and **B**) Structures of free 60S in the cytoplasm of untreated cells (A) and HHT-treated cells (B). ES27L and Ebp1 (PDB: 6SXO) are fitted into the 60S maps. Although Ebp1 was not confidently assigned to the 60S from untreated cells due to the lower resolution, it fitted better in comparison to alternative factors (amino-terminal acetyltransferases and nascent polypeptide-associated complex) binding to the tunnel exit. (**C**) Percentage of the 60S in untreated and HHT-treated cells normalized to the number of 80S ribosomes in the respective dataset. In untreated cells, abundance = 60S/(60S+80S) = 1,693/(1,693+39,402). In treated cells, 60S/(60S+80S) = 7,176/(7,176+39,070). (**D**) The structure of 60S in untreated cells fitted with PDB 6LSR indicates that eIF6 is missing (left), contrasting HHT-treated 60S (right). Large subunit GTPase 1 (LSG1), NMD3 and ZNF622 (PDB: 6LSR) are not observed in the HHT-treated 60S structure. (**E**) The PTC of free 60S from untreated and treated datasets fitted with PDB 6QZP. HHT is colored in cyan.

Science
AAAS

Supplementary Materials for

Translation dynamics in human cells visualized at high-resolution reveal cancer drug action

Huaipeng Xing[1,2], Reiya Taniguchi[1], Iskander Khusainov[1], Jan Philipp Kreysing[1,3], Sonja Welsch[4], Beata Turoňová[1], Martin Beck[1]*
Corresponding author: martin.beck@biophys.mpg.de

This PDF file includes:

Other Supplementary Materials for this manuscript include the following:

Materials and Methods

Cell culture

Flp-In T-Rex 293 cells (Invitrogen) were maintained in DMEM (Sigma) supplemented with 10% fetal bovine serum (Gibco) at 37°C with 5% CO2.

Cryo-ET sample preparation

R2/2 gold grids (200 mesh, Quantifoil) were glow discharged using a Pelco easiGlow device for 90 sec on both sides and placed in 3.5 cm cell culture dishes (MatTek). 2 ml cell suspension (175,000 cells/ml) was seeded in the dish containing grids and placed in the incubator. Cells without HHT treatment were cultured for 5 hours (h) before plunge freezing. For HHT (Santa Cruz Biotechnology) treatment, cells were cultured without HHT for 3 h and then treated with HHT at a final concentration of 100µM for 2 h before plunge freezing. For plunge freezing, grids were blotted from the backside for 6 sec using a Leica EM GP2 plunger at 70% humidity and 37°C, plunged into liquid ethane, and stored in grid boxes in liquid nitrogen. Plunge-frozen grids were FIB-milled under cryo-conditions with an Aquilos FIB-SEM (Thermo Scientific) as previously described (*49*). In brief, grids were coated with an organometallic platinum layer for 15 sec using a gas injection system. Cells were then stepwise milled using decreasing gallium ion-beam currents of 0.5 nA to 30 pA. In total, 35 cells were milled for the untreated sample and 32 for the HHT-treated sample.

Cell viability assay

Cell viability was measured using CellTiter-Glo 2.0 Cell Viability Assay (Promega) according to the manual. In brief, cells at a concentration of 175,000 cells/ml were cultured in 96-well plates. For treated cells, 100 µM HHT was added 3 hours after seeding (fig. S7B). 100µl of CellTiter-Glo. 2.0 Reagent was added at the corresponding time point (fig. S7B) and mixed for 2 minutes at room temperature. The luminescent signal was measured using a microplate spectrofluorometric reader (TECAN SPARK). Representative data from three repeated independent experiments are shown as mean ± standard deviation (SD). The statistical analysis was performed using two-tailed unpaired *t*-tests in GraphPad Prism. Previous work indicates that the impact of HHT on cell viability depends on the cell type, detection method and HHT treatment time: Beas-2b cells, 18 h, cytotoxicity concentration 50% (CC_{50}) > 10 µM (*50*); Huh7 cells, 48 h, CC_{50} = 0.0218 µM (*51*); Vero E6 cells, 48 h, CC_{50} = 59.75 µM (*52*); U937 cells, 48 h, CC_{50} > 0.1 µM (*53*). This makes CC50 less reliable than naturally expected (*54*).

BCA assay

The protein concentration was assessed with a bicinchoninic acid (BCA) assay kit (Thermo Fisher Scientific), following the standard protocol. For the untreated sample, cells were cultured in the 24-well plates for 5 h before measuring the protein concentration. For treated cells, HHT was added 3 h after seeding at a final concentration of 100µM. 2 h later, cells were lysed and the protein concentration was measured. Representative data from three repeated independent experiments were shown as mean ± standard deviation (SD). The statistical analysis was performed using two-tailed unpaired *t*-tests in GraphPad Prism.

Data acquisition

Tilt series were acquired on a Titan Krios G4 (Thermo Scientific) operated at 300kV and equipped with Selectris X imaging filter and Falcon 4 direct electron detector, at 4K x 4K pixel dimensions, pixel size of 1.188 Å, tilt range of -60° to 60°, 2° tilt increment, target defocus of -1.5 to -4.5 µm and a total dose of 120 to 150 e/Å^2 per tilt series, using SerialEM software (*55*). Target areas were selected in the cytoplasmic region of the cell (fig. S1A). All tilt series used in this study have been deposited in Electron Microscopy Public Image Archive (EMPIAR) (*56*).

Tomogram reconstruction and 80S ribosome template matching

Tilt series were aligned with patch-tracking in IMOD and reconstructed as back-projected tomograms with SIRT-like filtering of 10 iterations at bin4 (*57*, *58*). The alignment files were used for tomogram reconstruction in Warp 1.0.9 (*23*). In total, 358 tomograms were analyzed from untreated cells and 352 from HHT-treated cells. Template matching was performed with STOPGAP (*59*). For this, 1,080 potential 80S ribosomes from the untreated dataset and 1,031 from the HHT-treated dataset were manually picked and refined in RELION 3.1 as templates. Following the standard protocol of template matching (*59*), we used a 20-degree angular scanning step and the template was filtered to 30 angstroms. The parameters were set as follows: low-pass_sigma=3, high-pass filter radius=1, high-pass_sigma=2, calc_exposure=1, calc_ctf=1, apply_laplacian=0, noise_corelation=1, and a sphere mask with soft edge. Subsequently, subtomogram averaging was carried out using the Warp-M-RELION pipeline. The template matching results were visually checked in napari (*60*) (movie S1). To utilize all potential 80S ribosomes in the datasets, the coordinates with the top 800 constrained-cross-correlation (CCC) values in each tomogram were extracted as sub-tomograms in Warp. In total, 286,400 untreated ribosome sub-tomograms and 281,600 HHT-treated were reconstructed.

Refinement and model visualization

Sub-tomograms from template matching were classified and refined in RELION 3.1 (*61*). 39,402 particles from the untreated dataset and 39,070 from the treated dataset were assigned to the 80S ribosome class. Three repeats were performed with different initial references for comparison (figs. S3A and S9A). After refinement in RELION, multi-particle refinement of tilt series was performed in M 1.0.9 as previously described (*23*). Refinement of geometric and CTF parameters was performed sequentially. Fourier shell correlation (FSC) calculation and local resolution estimation were conducted in RELION and M. The untreated and treated 80S ribosomes structures reached ~3.2 Å resolution after the last refinement iteration in M. Density maps and molecular models were visualized using ChimeraX (*62*).

Subtomogram classification

To classify translation states, a tRNA mask and factor mask (fig. S2 and S8) with soft edge covering the tRNA path (A, P and E sites) and elongation factor binding sites were used sequentially in RELION 3.1 (*5*). First, 39,402 untreated and 39,070 HHT-treated ribosomes identified from the two datasets were classified with a tRNA mask (10 classes, T = 4, 35 iterations). Second, classification with a factor mask was performed using the following parameters: 3 or 5 classes, T = 4 or 5, 35 iterations. The ribosome classes with fewer than 500 particles were discarded after each round of classification because they could not be unambiguously assigned to specific states due to the low resolution. Five repeats were carried out to validate the classification with the same parameters mentioned above (figs. S3B and S9B). Further classification was performed with the elongation factor mask for the 'P' states from untreated and treated datasets, reducing the particle number from 1,892 to 1,777 for the untreated 'P' state and reducing the particle number from 4,198 to 3,990 for the treated 'P' state (figs. S2A and S8A). The 'eEF1A, A/T, P, E' state was further classified resulting in a sharper 40S subunit, and the particle number changed from 6,054 to 5,115. 'A/T, P' state was further classified (T=5, 2 or 3 classes, 35 iterations) with the mask focusing on the factor-like density but no new class was revealed. To further classify the 'eEF1A, A/T, P' state, a mask focusing on the elongation factor and A/T tRNA region was used (T=4 or 5, 3 or 5 classes, 35 iterations) but did not reveal any meaningful results. Finally, eight classes were identified in untreated cells and six classes were classified in treated cells. tRNAs (A, P, E and Z), eEF1A and eEF2 atomic models were obtained from PDB (6Z6M, 5LZS, 6MTB, 6TNU) and fitted into our density map of each state (*4*, *13–15*).

An elliptic mask covering both the potential membrane region and ES27L of the ribosome was used to classify the ribosomes with membrane, ES27L and Ebp1 (T = 4, 40 iterations). PDB

6SXO was rigid-body-fitted into our ribosome structures with Ebp1 (*30*). 654 membrane-bound ribosomes were identified. For validation, membrane-associated ribosomes were counted manually in tomograms containing membranes, showing a similar number as the classification. The results were also checked by mapping the identified membrane-bound ribosomes back into tomograms with ArtiaX in ChimeraX (*62*, *63*). A representative tomogram with membranes was segmented using Amira-Avizo 2021.1 (Thermo Scientific). The number of membrane-bound translation states is calculated by analyzing the shared particle coordinates between the membrane-associated ribosomes and individual translation states. First, the membrane-bound ribosome classification was carried out independently of the classification of the translation states. Then, each translation state was assigned to the membrane-associated ribosomes.

To classify the di-ribosome from the 39,402 untreated ribosomes, sub-tomograms were extracted with a bigger box size that could accommodate three ribosomes. After refinement in RELION 3.1, the classification was performed with a sphere mask focusing on the trailing ribosome (i+1). PDB 6I7O and 7QVP were fitted into our map (*26*, *27*) (fig. S17A).

Ribosome states analysis in individual tomograms and cells

After classification and refinement, 80S ribosome states were mapped back into their original tomograms for calculating their abundance. The tomograms were mapped back to the cells where they come from to represent the abundance of each cell's abundance of ribosome states. We analyzed 358 tomograms from 35 untreated cells and 352 tomograms from 32 treated cells. The heatmaps were prepared in GraphPad Prism. The single-cell clustering analysis was done in Matlab2019b with the clustergram function.

Polysome analysis

The refined positions obtained during the subtomogram averaging were used to trace the polysomes within tomograms. Since the coordinates correspond to the center of ribosomes, they were shifted to entry and exit points (see fig. S14B), resulting in two different sets of coordinates for each ribosome. For each tomogram, the polysome chains were traced using the routine described in table S4. The decision to append a ribosome to a chain was based solely on the distance between the exit point of the leading ribosome (denoted i) and the entry point of the trailing one (denoted i+1), i.e., the rotation of the trailing ribosome with respect to the leading one was not considered by the script. The ribosome with the shortest Euclidean distance (the nearest neighbor) to the leading ribosome was chosen to be the trailing one if it was within the allowed distance threshold. The distances from 2 to 25 nm were tested to determine the optimal threshold (figs. S14C and S15A). For each distance, the threshold was within the ±0.5 nm range (i.e., for 2 nm, the allowed distance was from 1.5 nm to 2.5 nm). The visual inspection of polysomes created with distances between 7 and 12 nm resulted in the threshold of 9 nm. The analysis of polysomes presented in this work corresponds to the distance threshold range from 0 to 9 nm. The polysome chain tracing was implemented in Python and will be publicly available on GitHub, together with Jupyter notebooks that were used to produce presented results.

Angle analysis of ribosome pairs

The distances and orientations between the neighboring ribosomes within polysomes were analyzed similarly to the previous study (*64*). Let $(\varphi, \theta, \psi)_i$ denote Euler angles describing the rotation of the reference to the leading ribosome *i* and let $(x, y, z)_i$ denote its coordinates. To analyze the angular relationships within the neighboring ribosomes, the leading ribosome *i* was rotated to the reference position (called zero rotation) by applying inverse rotation, i.e. it was rotated by $(-\psi, -\theta, -\varphi)_i$. The trailing ribosome i+1 was rotated by its rotation $(\varphi, \theta, \psi)_{i+1}$, followed by a rotation of $(-\psi, -\theta, -\varphi)_i$. This brings the ribosome pair into a common rotation frame (zero rotation of the leading ribosome) while keeping their original angular relationship. The relative orientations of the ribosomal pairs within polysomes were shown in figs. S15D and S17D. For the

distance analysis, the exit site coordinates of a leading ribosome were subtracted from both the leading ribosome's exit site coordinates (setting it to zero) and its trailing ribosome's entry site coordinates. The new entry site coordinates of the trailing ribosome were rotated by $(-\psi, -\theta, -\varphi)_i$ to show their position with respect to the zero rotation of the leading ribosome (fig. S15C).

Visual analysis of the neighboring pairs revealed three abundant orientations (fig. S17, B and C). Five representative pairs from each observed group were analyzed to determine their angular relationship. The top-top (t-t) orientation corresponds to the angular difference (*65*) of roughly 90 degrees. The top-down (t-d) and top-up (t-u) have both angular differences of around 115 degrees. The t-d and t-u pairs can be further distinguished by the difference in their φ angles – for t-d the difference is above 100 degrees and for t-u it is below 0 degrees (the Euler angles are always expressed in their canonical form, which yields range ±180 degrees for φ and ψ, and 0 – 180 degrees for θ). Applying these restrictions (with the tolerance of ±10 degrees) onto neighboring pairs within polysomes yielded the following distribution (fig. S17, D and E): 40.9% (t-t), 16.2% (t-d) and 4.5% (t-u) in the untreated dataset and 34.8% (t-t), 0.5% (t-d) and 9.5% (t-u) for the treated dataset.

Free 60S and 40S template matching, classification and refinement

We processed the 60S and 40S similarly to the 80S ribosome (see above). After template matching of free 60S and 40S, several rounds of classification (3 or 4 classes, T = 1, 30 iterations) were performed in RELION 3.1 (*5*). 1,693 60S and 1,682 40S were classified in untreated cells. 7,176 60S and 3,895 40S were classified in HHT-treated cells. The refinement was performed in RELION3.1 and M 1.0.9.

Supplementary figures

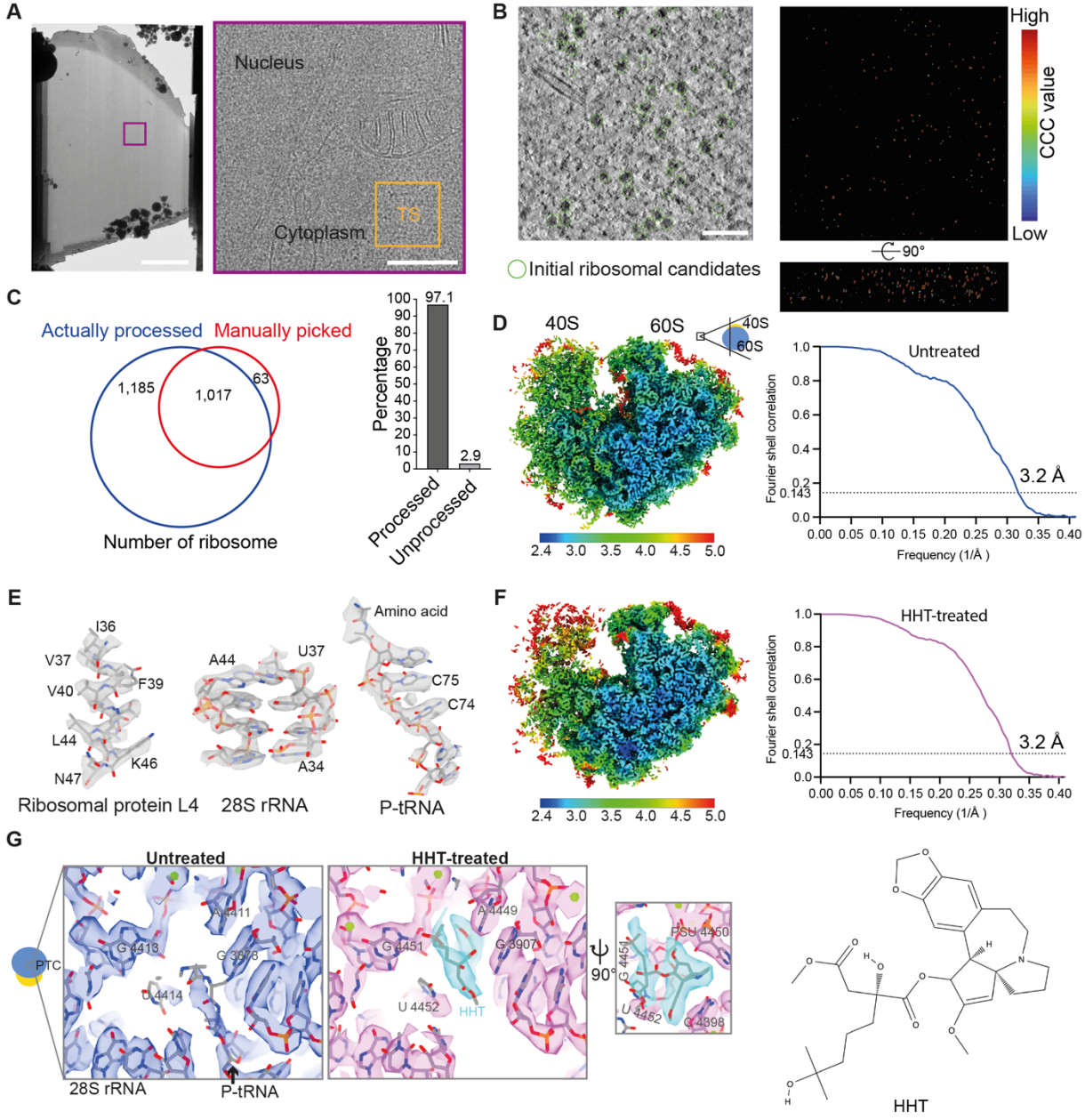

Fig. S1. Untreated and HHT-treated ribosome maps in human cells.

(**A**) Transmission electron micrographs of FIB-milled lamellae. Scale bar, 4 µm (left panel); 500 nm (right panel). The orange square indicates a representative region used for data collection. TS denotes tilt series. (**B**) A tomogram slice from an untreated cell. Top 800 potential ribosomes (green circles) per tomogram were selected based on the constrained cross-correlation (CCC) value of template matching for the following classification (left). CCC values from the template matching (right, see also movie S1). (**C**) Evaluation of manually picked and template matched ribosomes. 1,080 potential ribosomes (red cycle) were manually picked from 10 tomograms. In the same 10 tomograms, 2,202 ribosomes (blue cycle) were template matched (see fig. S2). 63 out of 2,202 (2.9%) of manually picked ribosomes were not template matched (right panel). (**D**) 80S ribosome determined from 39,402 particles from untreated cells and the map colored by local resolution. The Fourier shell correlation (FSC) curve of the untreated ribosome reveals an overall

resolution of ~3.2 Å using the 0.143 criterion. (**E**) Structures of ribosomal protein L4, 28S rRNA and P-tRNA from untreated cells fitted with PDB 5AJ0. (**F**) The structure of the ribosome determined from 39,070 particles under HHT treatment. The map is colored by local resolution. 40S was less resolved possibly owing to the heterogeneity of particles (see Fig. 2, half population of the treated ribosome with unrotated small subunit and half with rotated). The FSC curve for the HHT-treated ribosome (right). (**G**) The PTC of ribosomal averages from untreated and HHT-treated cells (see also movie S2). The untreated ribosome was fitted with PDB 5AJ0. The treated ribosome was fitted with PDB 6QZP. The black arrow indicates P-tRNA. Green sphere, potential Mg^{2+}. The chemical structure of HHT (right).

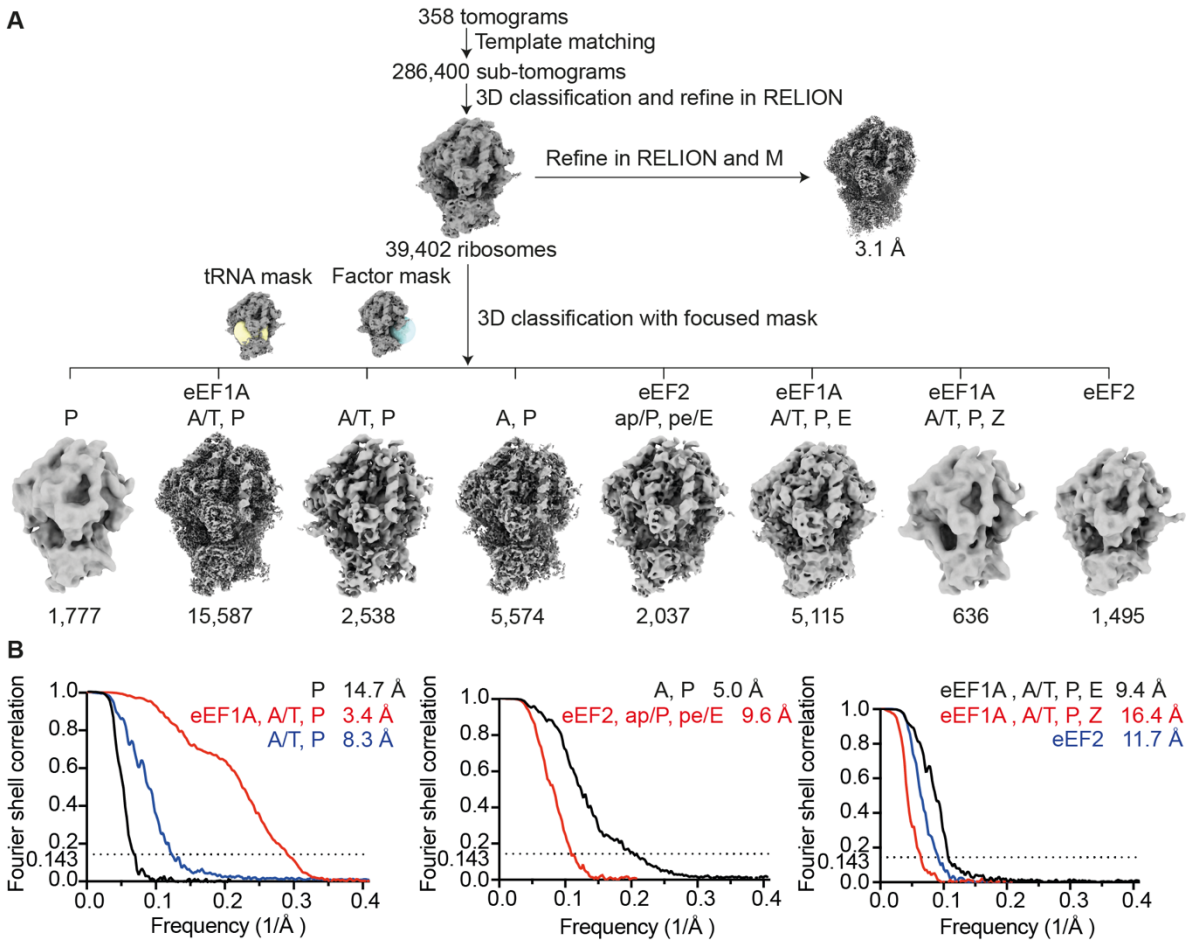

Fig. S2. Image-processing workflow for the dataset of untreated cells.

(**A**) Diagram of the cryo-ET data analysis workflow of ribosomes in untreated cells. Template matching in STOPGAP generates 286,400 ribosome candidates. Classification in RELION identified 39,402 ribosomes after removing false positive particles. Classified ribosomes were refined in RELION and M. A focused classification was performed with a tRNA mask covering the tRNA path and a factor mask focusing on the elongation factor binding area. Finally, eight ribosome states were determined. (**B**) FSC curves of the corresponding ribosome structures and the resolution were provided (FSC = 0.143).

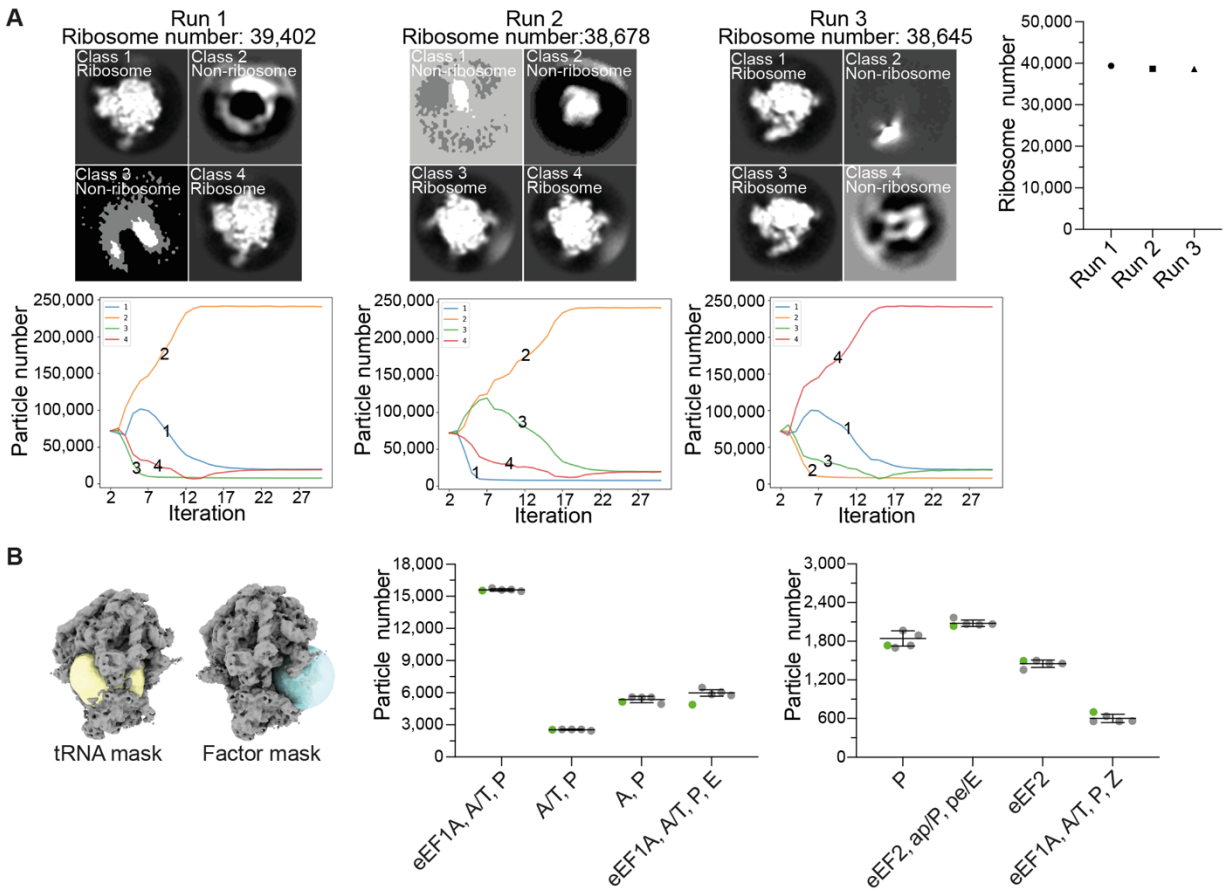

Fig. S3. Validation of ribosome classification in native untreated cells.

(**A**) Output of three runs to classify ribosomes using different initial references after template matching in untreated cells. In each run, the total number of the classified ribosome was summarized (top right). The curves show the change in the particle number of each class over 30 iterations (bottom panel). The first run was used for the following processing. (**B**) Five repeats of the focused classification with the indicated masks using the same parameters. The repeat marked with green dots was used to calculate the percentage in Fig. 2 and the final refinement in RELION and M.

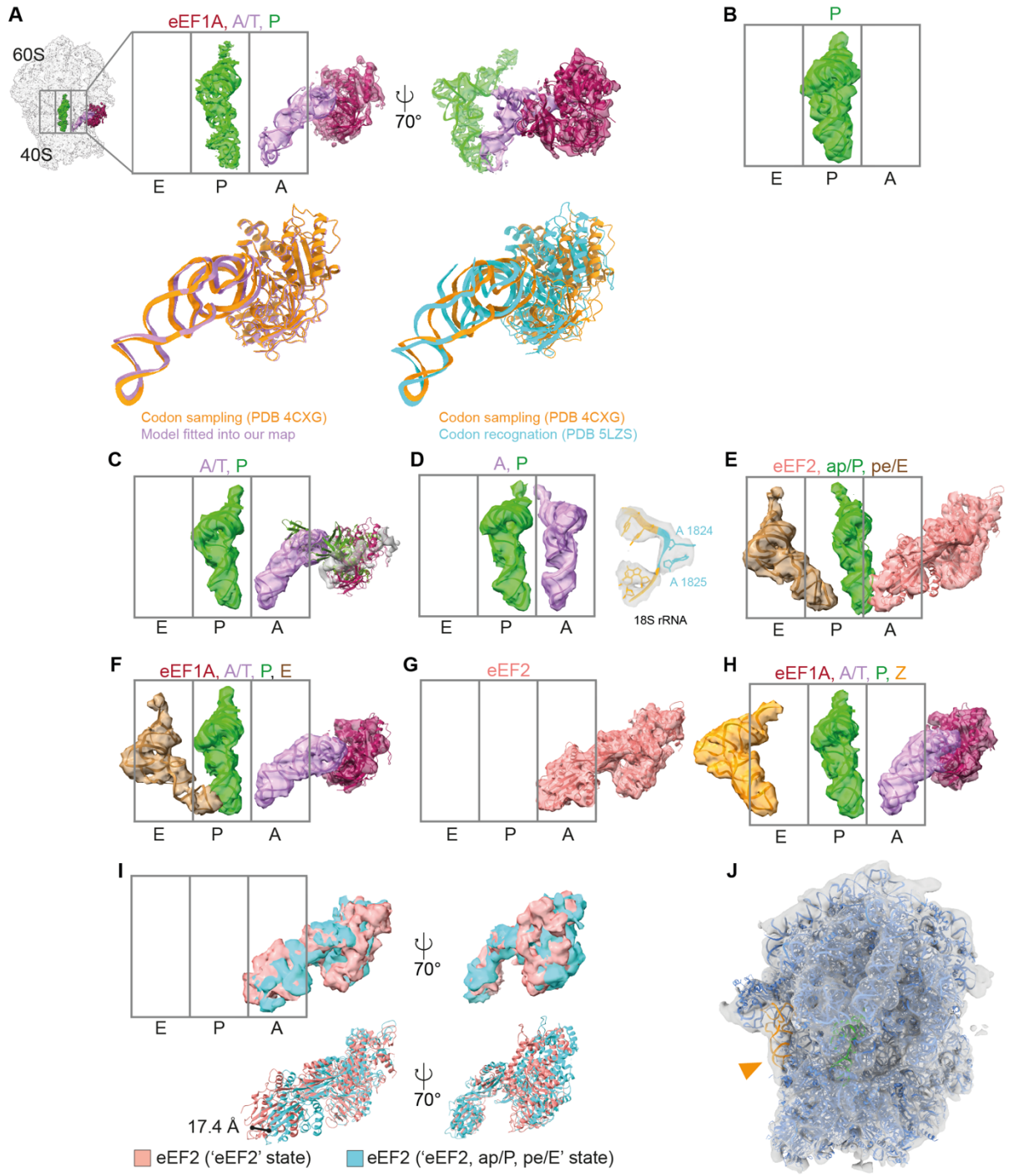

Fig. S4. Atomic models of tRNAs and elongation factors fitted into the map of the untreated ribosome.

(**A** to **H**) The densities of tRNAs, eEF1A and eEF2 from eight ribosome states were rigid-body-fitted with the previously determined atomic model (Materials and methods). The fitted models represent the averaged positions of the nearby tRNA and the elongation factor. Colors: eEF1A (maroon), eEF2 (salmon), A and A/T (lavender), P and ap/P (green), E and pe/E (brown), Z (tangerine). (**A**) Comparison of the codon sampling states from PDB 4CXG (orange) and this study (lavender, by fitting 4CXG) (bottom left). Superposition of codon sampling state (PDB 4CXG,

orange) onto the codon recognition state (PDB 5LZS, cyan) (bottom right). (**C**) The model of eEF1A at the extended (PDB 8B6Z, fern) or the compact conformation (PDB 5LZS, maroon) did not fit well into the factor-like density (gray) of the 'A/T, P' state. (**D**) The atomic model (PDB 5LZS) of 18S rRNA (A1822 to A1827) was rigid-body-fitted into the corresponding density of the 80S at the 'A, P' state. The decoding nucleotides A1824 and A1825 in the atomic model were in the flipped-out configuration (right panel). (**I**) The difference in eEF2 position between the 'eEF2, ap/P, pe/E' state (cyan) and the 'eEF2' state (salmon). The 80S ribosome maps of the two states were superimposed, and the eEF2 model from PDB 6Z6M was fitted into both maps. (**J**) The atomic model of the 'P, Z' state ribosome (PDB: 6MTB) was fitted into the map of the 'eEF1A, A/T, P, Z' state from untreated cells. Tangerine, Z-tRNA.

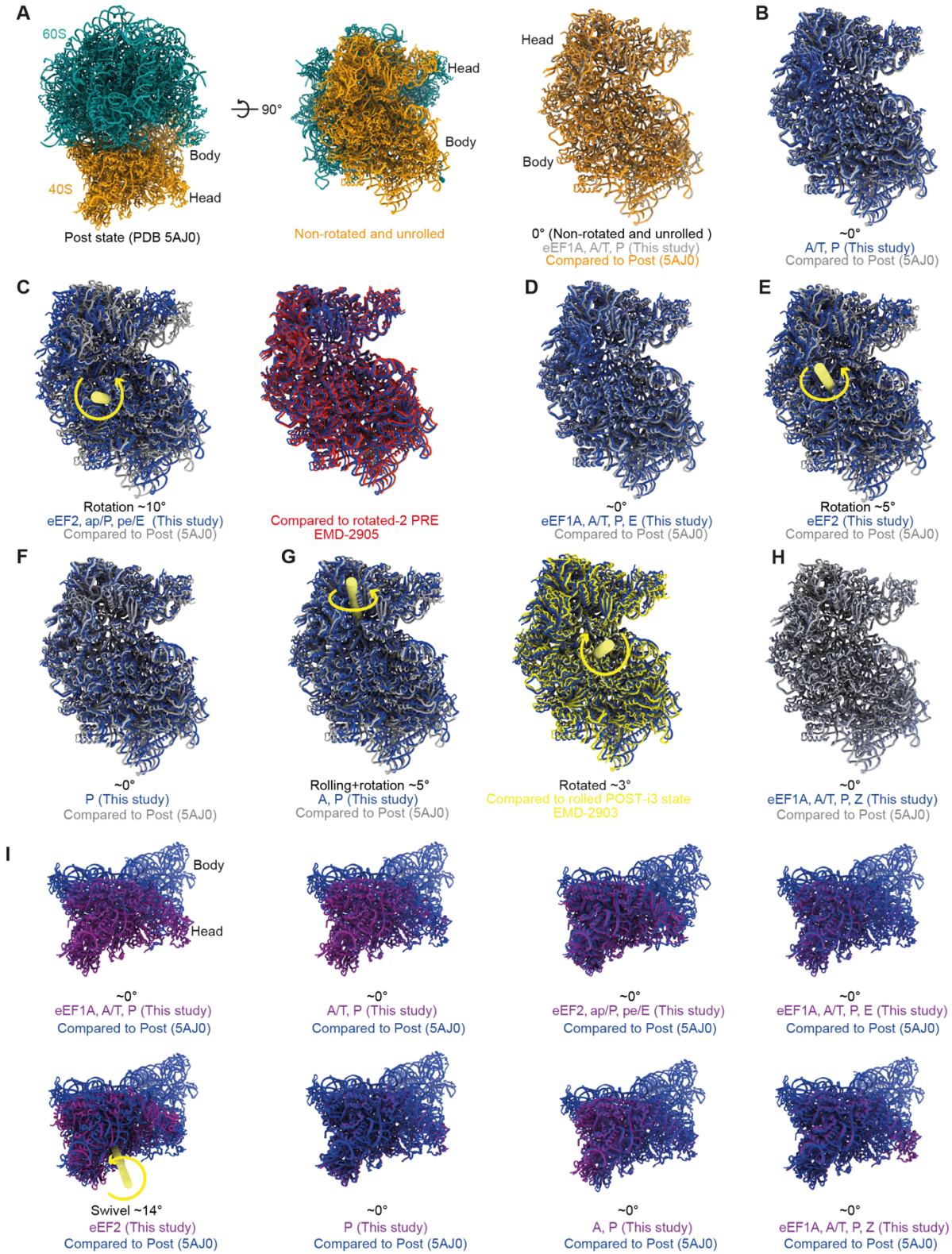

Fig. S5. Analysis of small subunit rolling, rotation and head swivel in untreated cells. (**A** to **H**) All superimposed structures were aligned based on the large subunit. Atomic model of unrotated and unrolled 80S ribosome from PDB 5AJ0 (A, left panel). The rolling and rotation of the 40S of all ribosome states (B to H, blue) in untreated dataset compared to unrotated/unrolled PDB 5AJ0 (B to H, gray). (**C**) Comparison of the position of 40S of 'eEF2, ap/P, pe/E' to

rotated-2 PRE (EMD-2905, red) (right panel). (**G**) Comparison of the position of 40S of 'A, P' to rolled POST-i3 (EMD-2903, yellow) indicates ~3° rotation (right panel), suggesting the 40S of the 'A, P' state was rolled and rotated compared to the POST state (PDB 5AJ0, left panel). (**I**) Comparison of 40S head swivel in this study (purple) to PDB 5AJ0 (blue) based on the alignment of 40S body. Significant 40S head swivel was only observed in 'eEF2' state. Models of 60S, 40S head and body (from PDB 5AJ0) were rigid-body-fitted into our ribosome maps at the indicated states. The rotation/rolling/swivel angles were measured in ChimeraX. The arrow and stick indicate the rotation/rolling/swivel direction and axis.

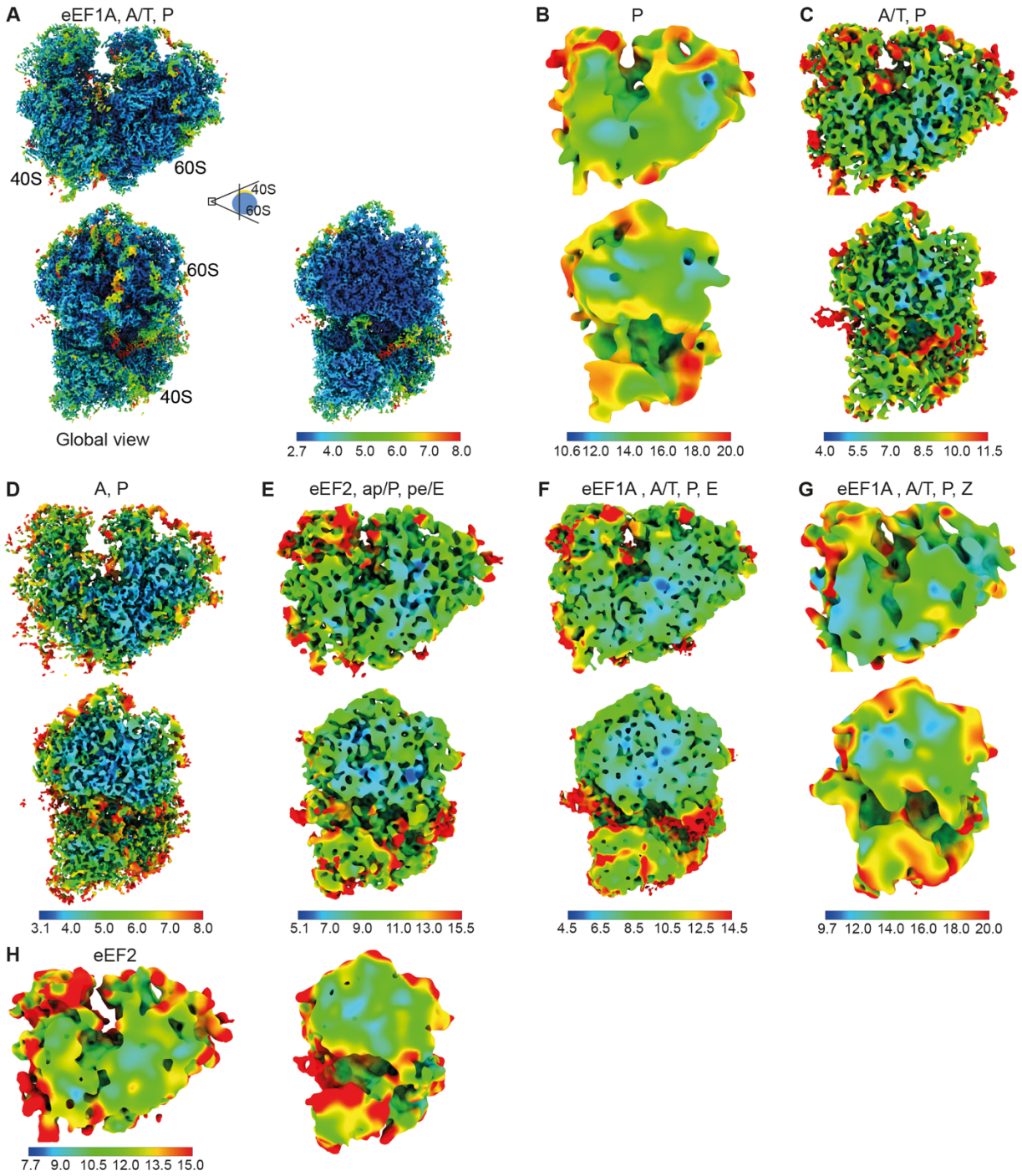

Fig. S6. Local resolution maps for ribosome classes in the untreated dataset.

(**A** to **H**) Eight ribosome states identified in the untreated dataset displayed as color-coded local resolution maps calculated in M. Color keys are shown below each panel.

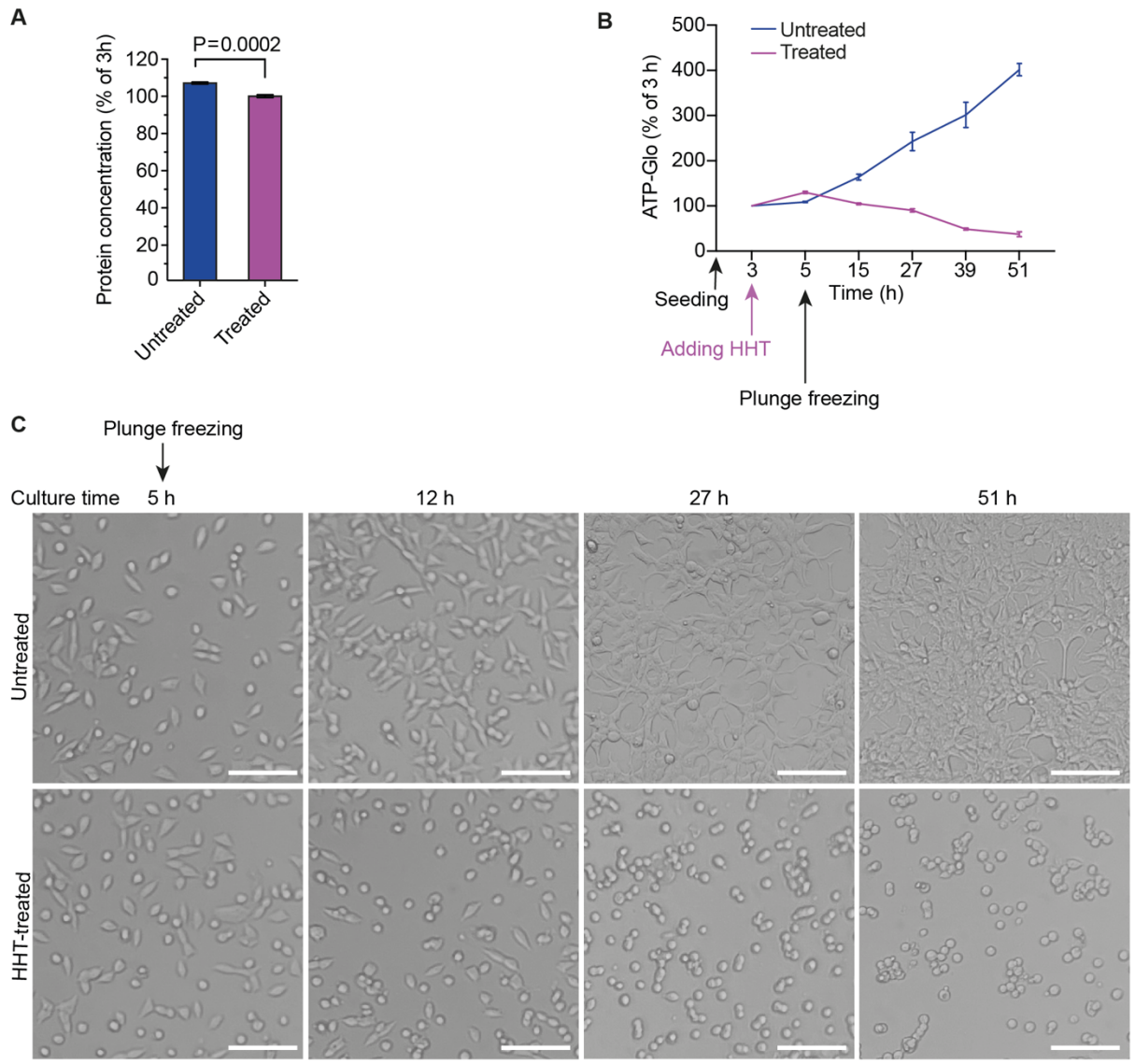

Fig. S7. The impact of HHT on protein expression and cell viability.

(**A**) Relative protein concentration 5 h after seeding (the same time point when we did plunge freezing) in untreated and HHT-treated cells. For treated cells, 100 μM HHT was added 3 h after seeding. The protein concentration at 3 h after seeding was set to 100%. The data represent the mean ± SD of three independent experiments. Statistical analysis was performed using two-tailed unpaired *t*-tests in GraphPad Prism. Significantly different ($P < 0.05$). (**B**) Cell viability was assessed by the ATP level in the cells at corresponding time points. For treated cells, 100 μM HHT was added 3 h after seeding. The ATP signal at 3 h after seeding was set to 100%. The data represent the mean ± SD of three independent experiments. (**C**) Cell morphology at different time points with or without HHT treatment. The top panel shows untreated cells 5 h to 51h after seeding as control. The bottom panel shows cells treated with 100 μM HHT. The drug was added 3 h after seeding, meaning the drug treatment time is 2 h, 9 h, 24 h or 48 h from left to right. Scale bar, 100 μm.

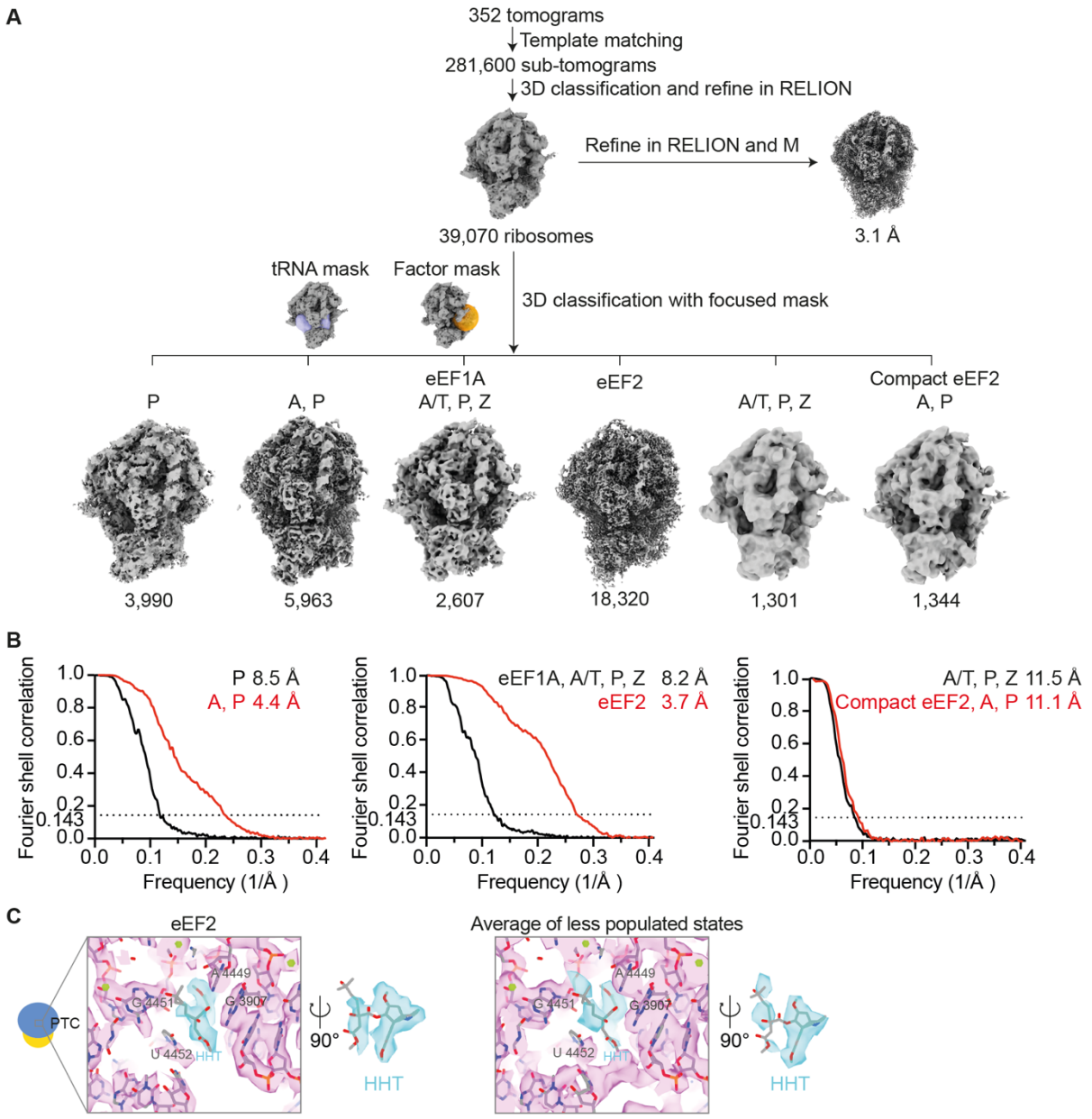

Fig. S8. Data-processing workflow for the HHT-treated cells.

(**A**) Diagram of the cryo-ET data analysis workflow of ribosomes in HHT-treated cells. Template matching in STOPGAP generates 281,600 ribosome candidates. Classification in RELION identified 39,070 ribosomes after removing false positive particles. Classified ribosomes were refined in RELION and M. A focused classification was performed with a tRNA mask covering the tRNA path and a factor mask focusing on the elongation factor binding area. Six ribosome states were detected. (**B**) FSC curves of corresponding ribosome states and the resolution are provided (FSC = 0.143). (**C**) The peptidyl transferase center (PTC) of ribosomes from HHT-treated cells. The HHT structure of the 'eEF2' state (left panel). The HHT structure of the 'A, P' state is shown in Fig. 3B. The average map of the four less abundant classes (right panel): 'P', 'eEF1A, A/T, P, Z', 'A/T, P, Z' and 'Compact eEF2, A, P'. PDB 6QZP was rigid-body-fitted into the above map. HHT is colored in cyan.

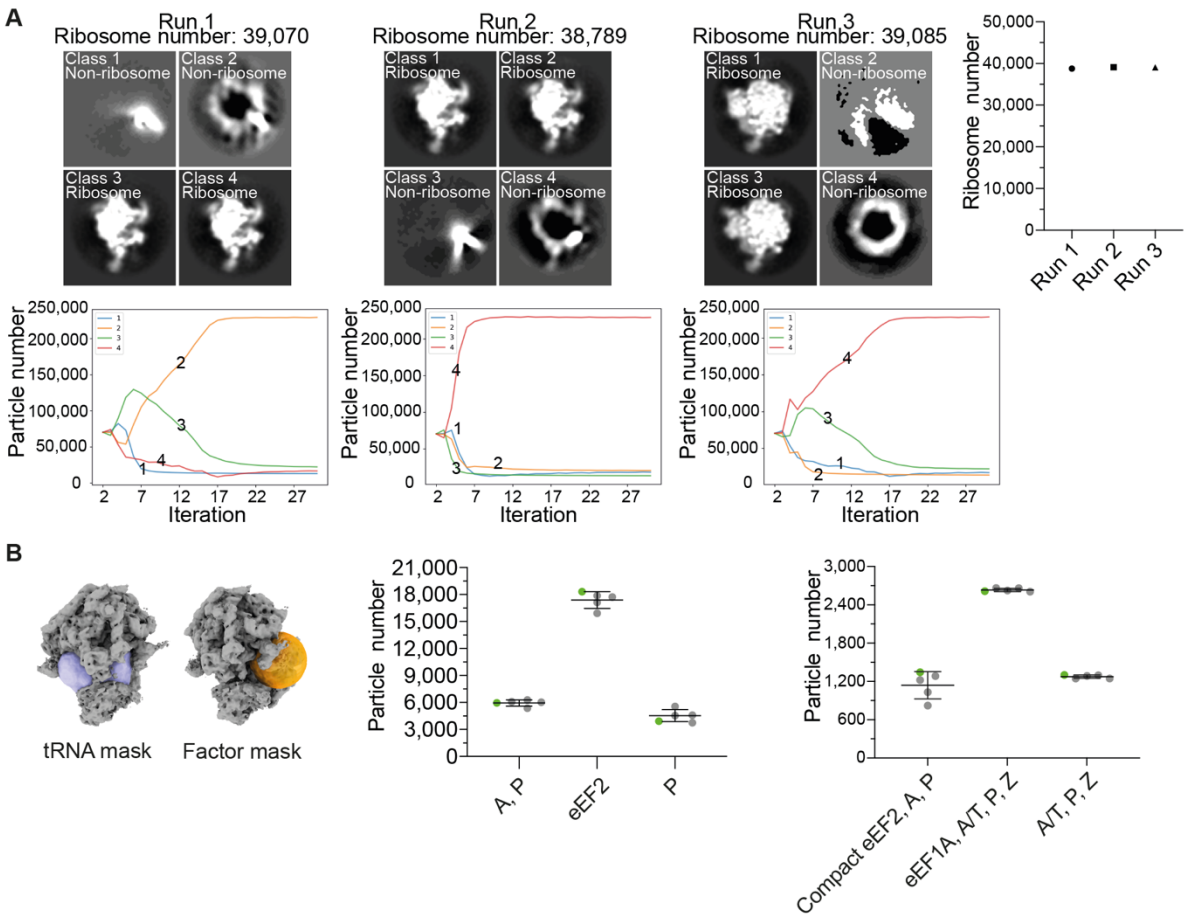

Fig. S9. Validation of ribosome classification from HHT-treated cells.

(**A**) Output of three runs of classification to identify ribosomes after template matching in HHT-treated cells. The total number of the classified ribosomes is shown in the top-right panel. The curves show the change in particle number of each class over 30 iterations (bottom panel). The first run was used for the following classifications. (**B**) Five repeats of the classification with masks focusing on the tRNA path and elongation factor binding site. One of the repeats marked with green dots was used for the final refinement in M and for calculating the percentage in Fig. 2.

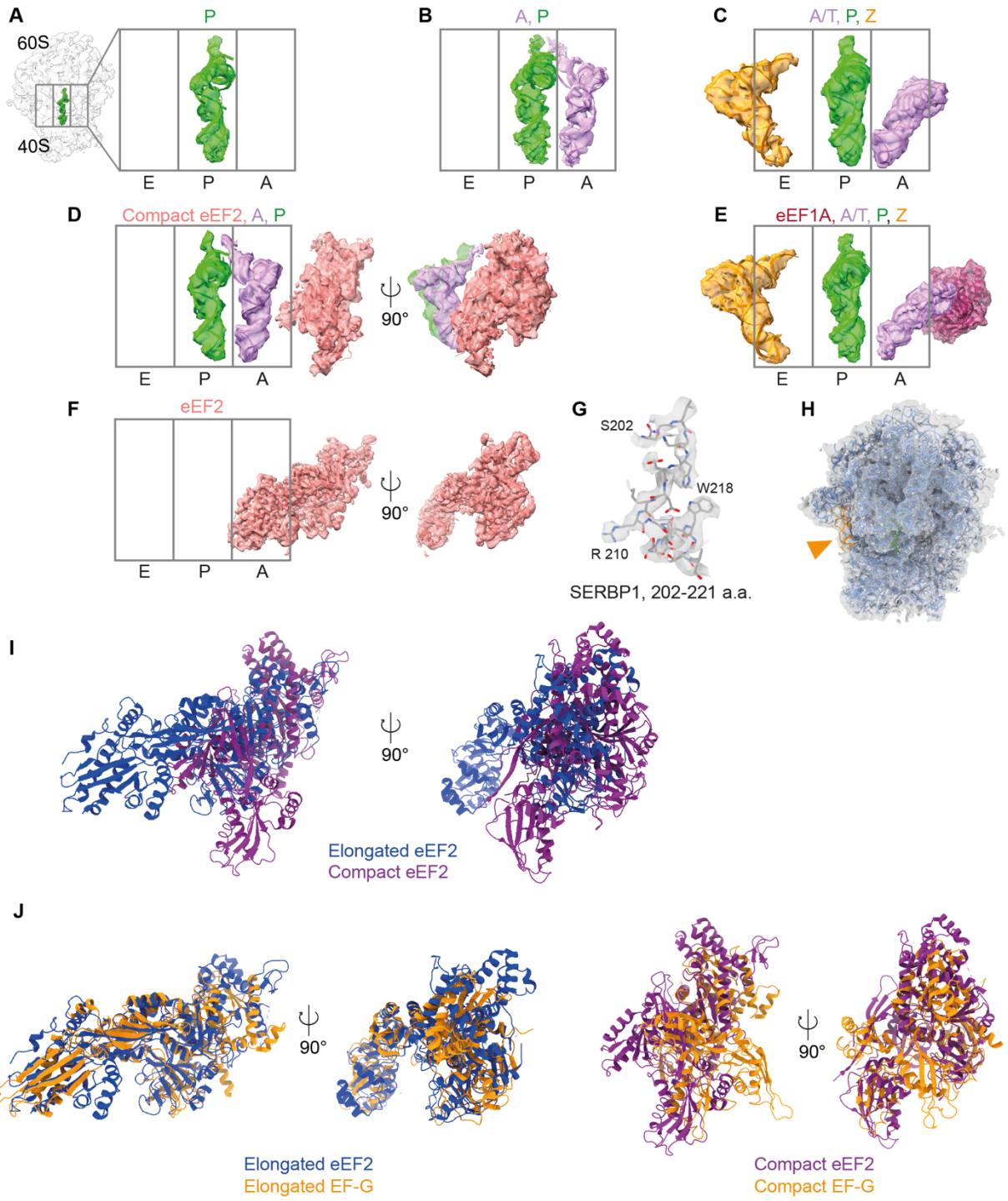

Fig. S10. Atomic models of tRNAs and elongation factors fitted into the corresponding densities of the treated ribosomes.

(**A** to **F**) The densities of tRNAs and elongation factors were fitted with the previously determined atomic model (Materials and methods). Colors: eEF1A (maroon), eEF2 and compact eEF2 (salmon), A and A/T (lavender), P (green), E (brown), Z (tangerine). In (D), five individual domains of eEF2 (PDB: 6Z6M) were rigid-body-fitted into the density of compact eEF2. (**G**) The atomic model of SERBP1 (202-221 amino acids) from PDB 6Z6M was fitted in the 'eEF2' map. No densities of eIF5A and coiled-coil domain containing short open reading frame 124

(CCDC124) were found in the ‘eEF2’ state. (**H**) PDB 6MTB was fitted into the ‘eEF1A, A/T, P, Z’ state maps (see also movie S3). Tangerine, Z-tRNA. (**I**) Elongated eEF2 (PDB 6Z6M) was superposed onto the compact eEF2 in (D). (**J**) The left panel shows the structural superposition of elongated eEF2 (PDB 6Z6M) and elongated EF-G (PDB 4WQF). The right panel shows the overlay of the structures of compact eEF2 in (D) and compact EF-G (PDB 4WPO).

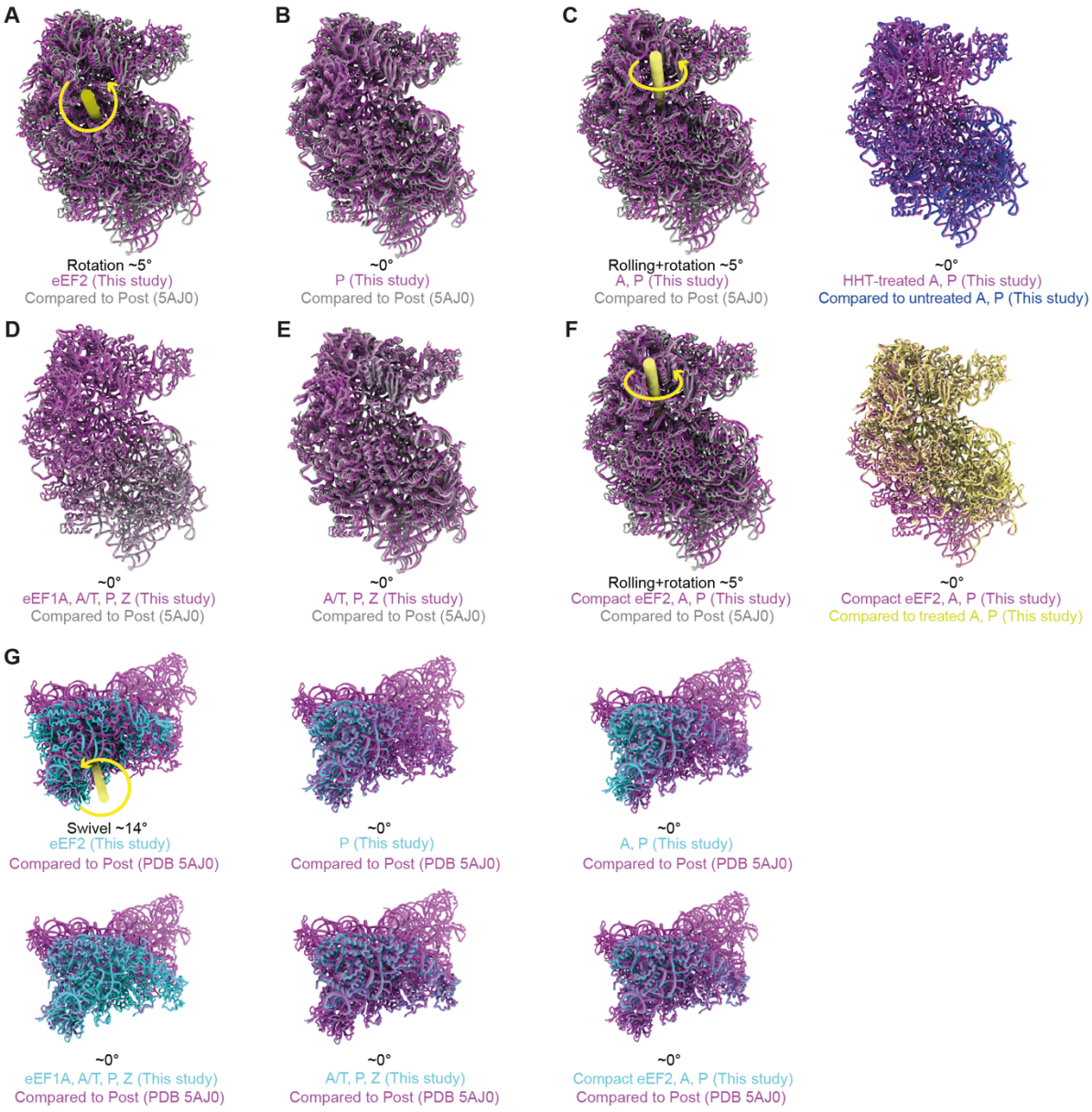

Fig. S11. Analysis of small subunit rolling, rotation and head swivel in HHT-treated cells. (**A** to **F**) Comparison of the small subunit rolling and rotation in HHT-treated dataset (magenta) to PDB 5AJ0 (gray) based on the alignment of the large subunit. (**C**) The 40S positions of untreated and treated 'A, P' are similar. (**F**) The 40S positions of 'A, P' and 'compact eEF2, A, P' are not distinguishable. (**I**) Comparison of 40S head swivel in this study (cyan) to PDB 5AJ0 (magenta) based on the alignment of 40S body. Significant 40S head swivel was only observed in 'eEF2' state. The analysis was done the same as fig. S5.

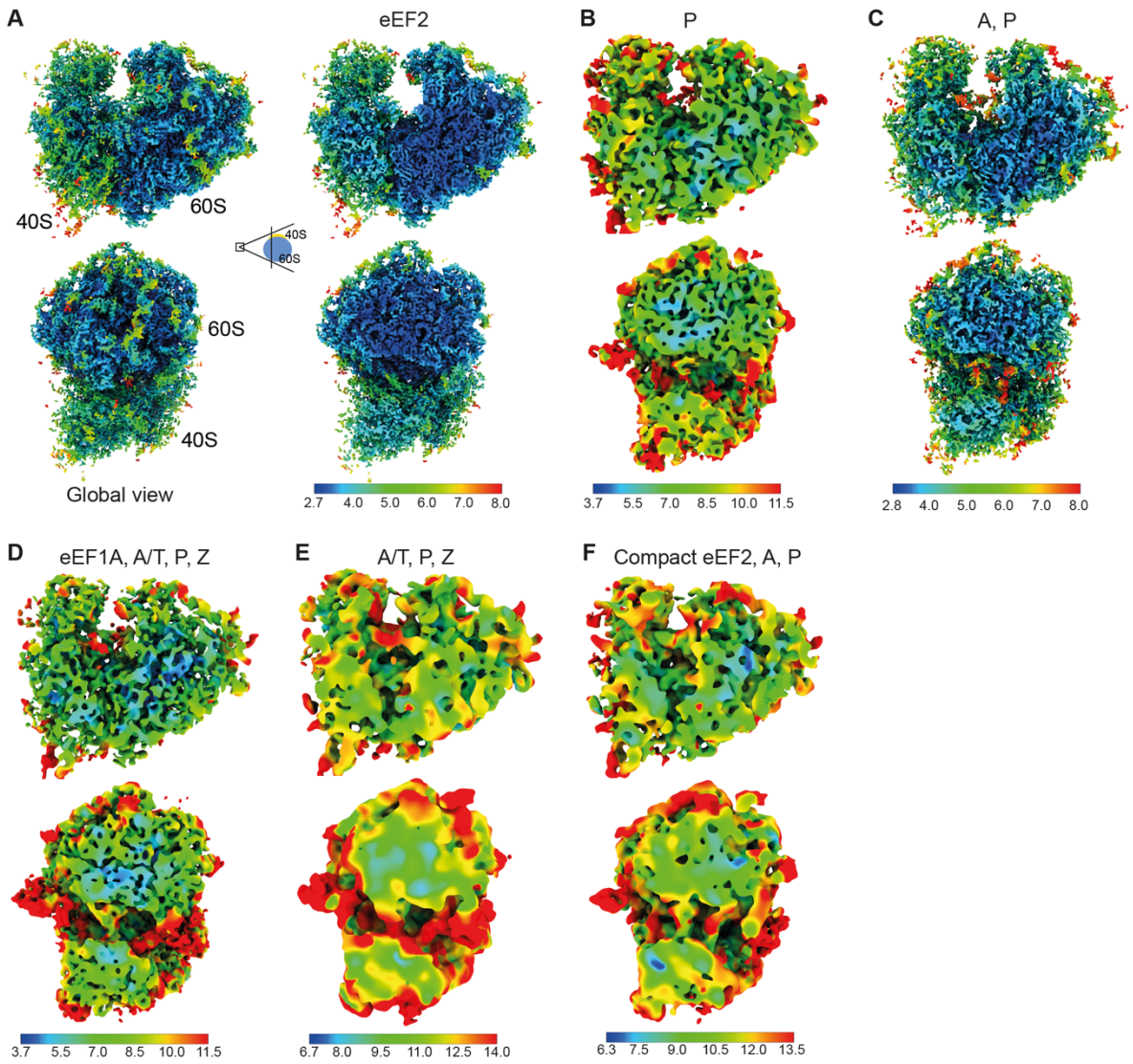

Fig. S12. Local resolution maps for ribosome classes from the treated cells.
(**A** to **G**) Six ribosome states colored by local resolution calculated in M. Color keys are shown in the bottom.

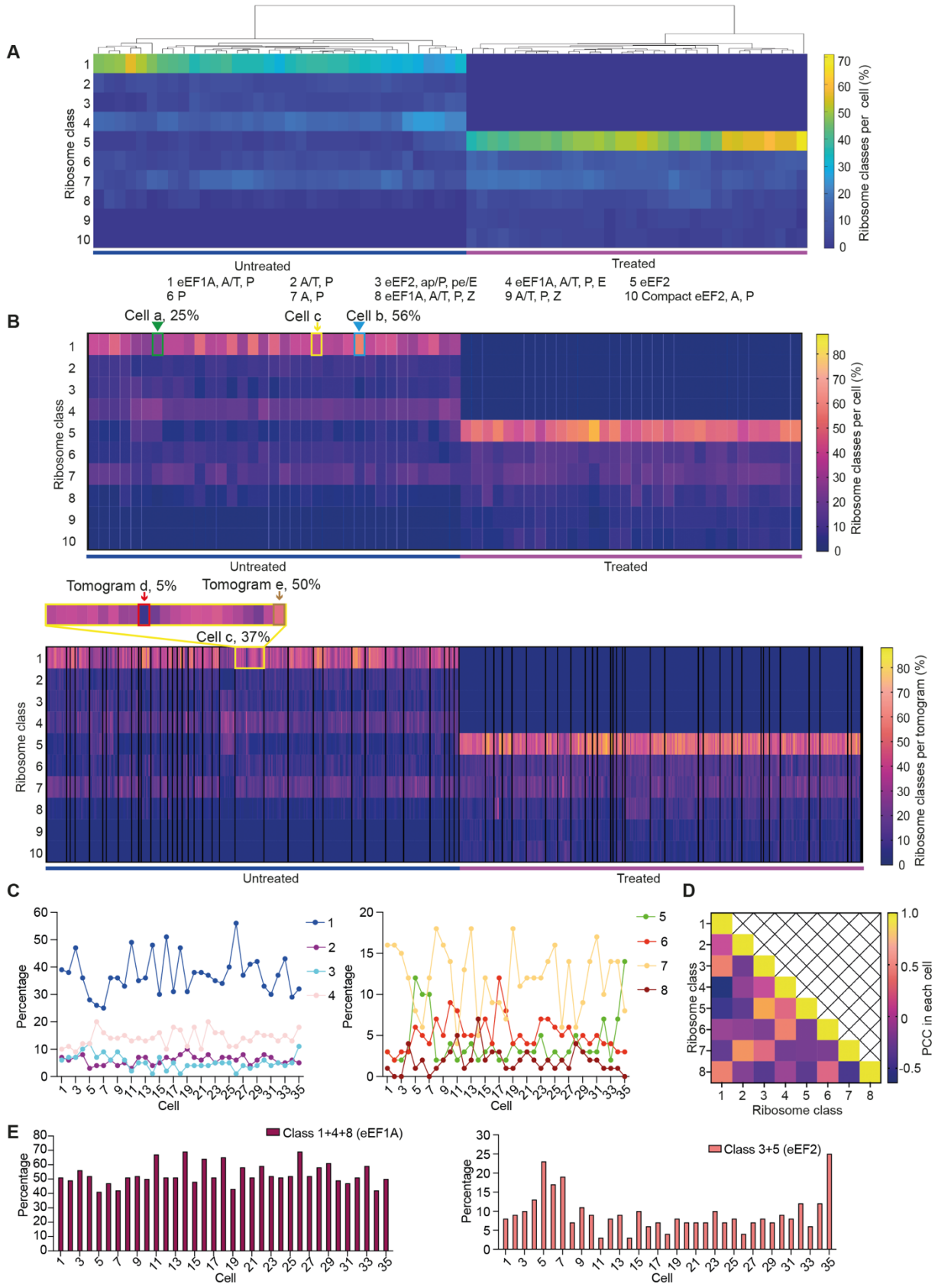

Fig. S13. Analysis of ribosome states in individual cells.

(**A**) Hierarchical clustering analysis of ribosome states in 35 untreated and 32 HHT-treated cells. Each column represents one cell. The analysis was done using clustergram in MATLAB 2019b. **(B)** Heat map of individual ribosome states from the untreated dataset (35 cells, 358 tomograms) and treated dataset (32 cells, 352 tomograms). Each column represents one cell (top heatmap) or one tomogram (bottom heat map). Black lines divide the tomograms from different cells (bottom heatmap). The class number is the same as in (A). Percentage of 'eEF1A, A/T, P' state: ~25% in cell a (green triangle, the lowest in the dataset), ~56% in cell b (blue triangle, the highest in the dataset), ~37% in cell c (yellow arrow), ~5% in tomogram d (red arrow), ~50% in tomogram e (brown arrow). Tomograms d and e are from the same cell c. (**C**) The abundance of eight ribosome states in individual untreated cells. (**D**) Pearson's correlation coefficient of ribosome states in the same cell (35 untreated cells). The input is the corresponding percentage in (C). The class number is the same as in (A). (**E**) Percentage of ribosome states containing eEF1A or eEF2 in individual cells.

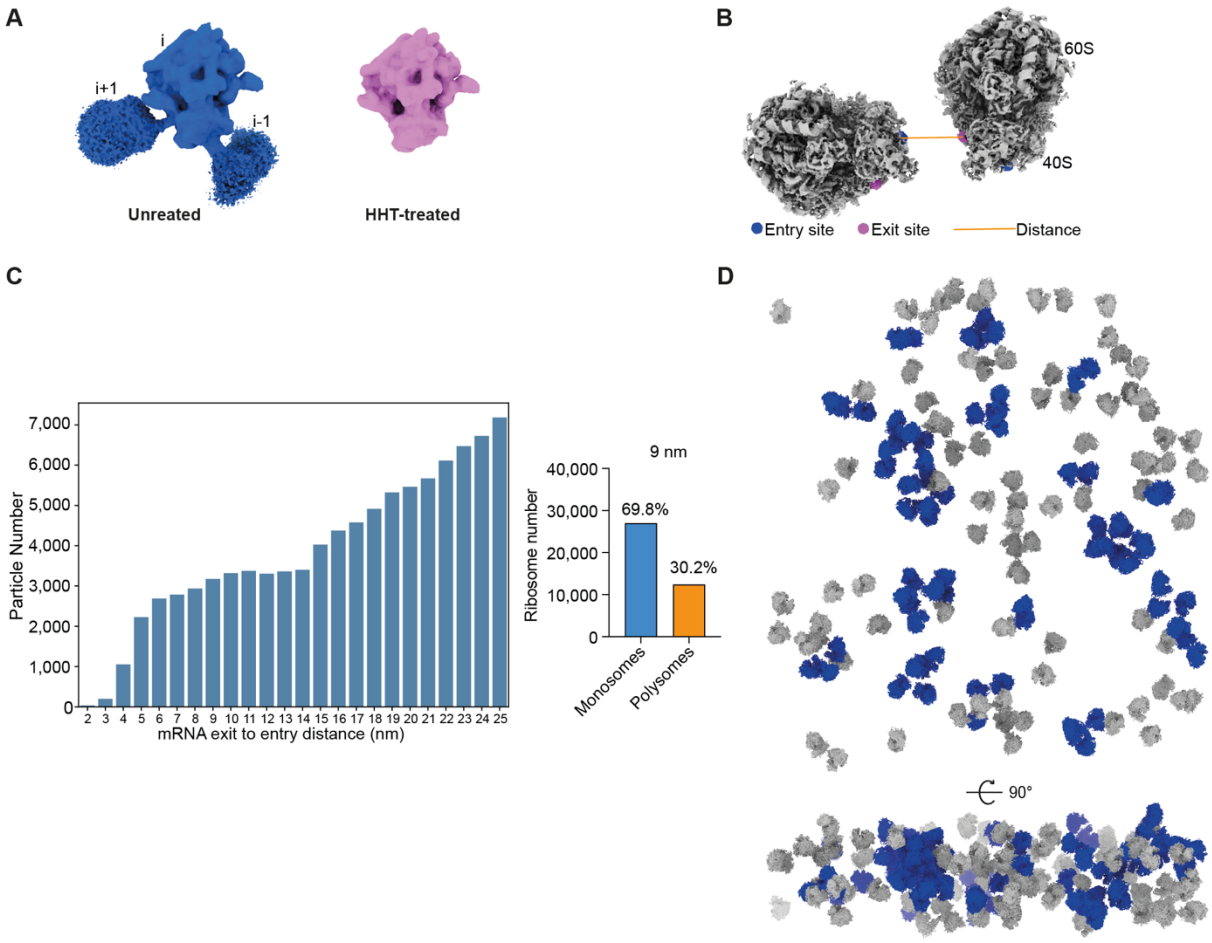

Fig. S14. Polysome analysis in the untreated dataset.

(**A**) Subtomogram average map of 39,402 untreated ribosomes (left) and 39,070 HHT-treated ribosomes (right) depicted at similar contour level. The treated ribosome can have a little neighboring density at lower contour level. i, the potential leading ribosome. i+1, the potential trailing ribosome. (**B**) Graphic of the polysomes detection method based on the distance from the mRNA exit site of one ribosome to the entry site of the other ribosome (short for exit-to-entry distance). (**C**) The numbers of detected polysomes within 2 to 25 nm (exit-to-entry distance) proximity in untreated cells (left). The abundance of monosomes and polysomes using the cut-off of 9 nm (right). (**D**) A tomogram showing the detected monosomes (grey) and polysomes (blue).

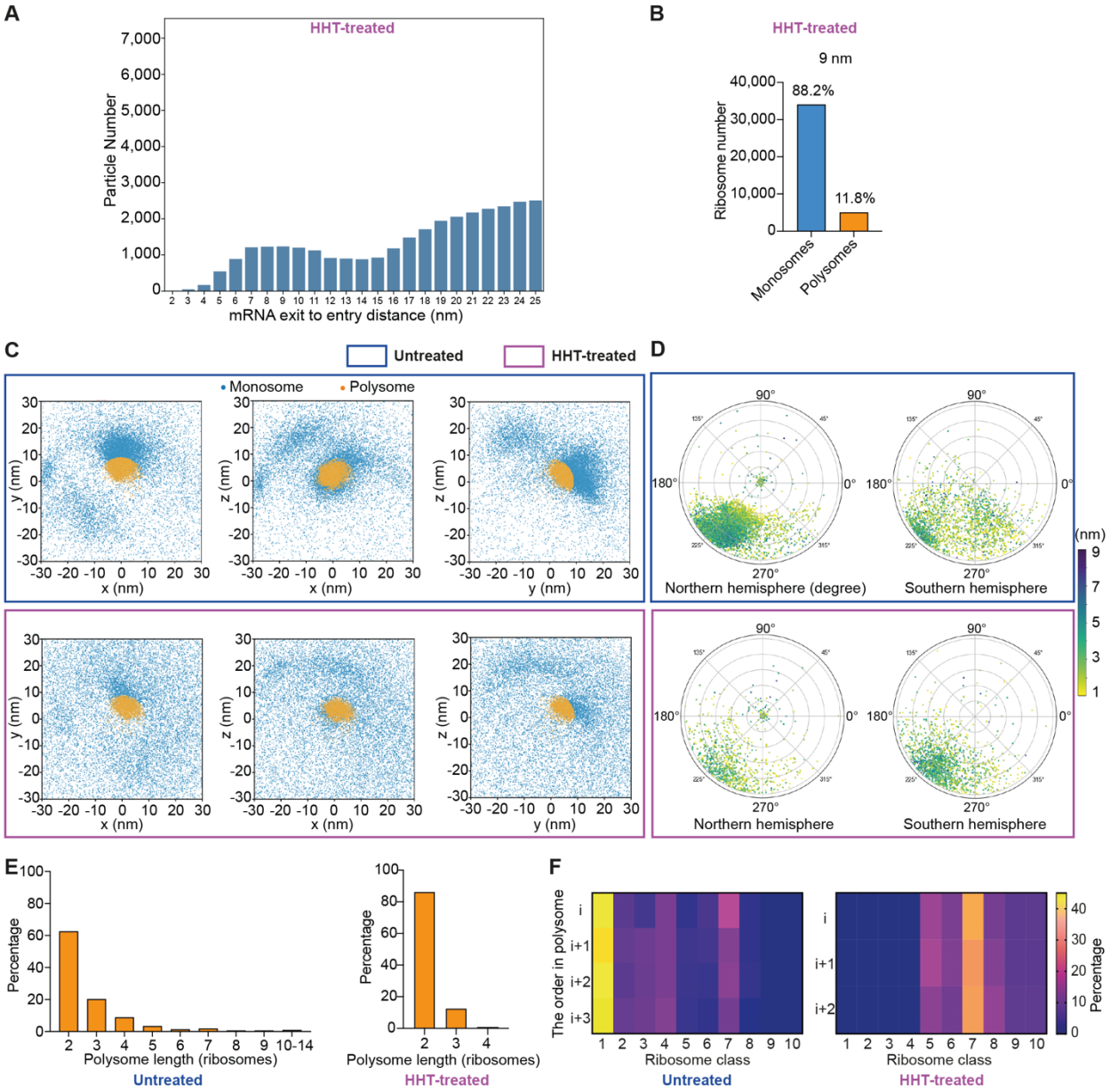

Fig. S15. Comparison of polysomes between treated and untreated cells.

(**A**) The numbers of detected polysomes within 2 to 25 nm (exit-to-entry distance) proximity in HHT-treated cells. (**B**) The abundance of monosomes and polysomes using the cut-off of 9 nm. (**C**) Distribution of the nearest neighboring ribosomes within 30 nm (exit-to-entry distance) in untreated (top) and treated cells (bottom). The positions of the entry sites of trailing ribosomes were normalized to the exit sites of the leading ribosome positions (these correspond to 0 in all dimensions) and rotated by the inverse rotation of the respective leading ribosomes. The positions corresponding to the ribosomes within polysomes are colored orange, and blue corresponds to monosomes. (**D**) Angular distribution of the trailing ribosomes in polysomes in untreated (top) and treated cells (bottom). The points represent cone rotation (described by Euler angles θ and ψ) of vector (0, 0, 1), projected on the northern hemisphere (for rotated vectors with z coordinate > 0) and southern hemisphere (for rotated vectors with z coordinate <= 0) using stereographic projection. The north pole corresponds to zero rotation, i.e. to a vector (0, 0, 1). The rotations of trailing ribosomes were multiplied by the inverse rotations of the respective

leading ribosomes. The points are color-coded based on the Euclidean distance between the leading ribosome exit site and the trailing ribosome entry site. (**E**) Distribution of polysome length in untreated (left) and treated cells (right). (**F**) The ribosome states distribution in i, i+1, i+2 or i+3 in polysomes. i, the leading ribosome. i+n, the trailing ribosome. Left, untreated cells. Right, treated cells. The ribosome class is the same as in Fig. 3A.

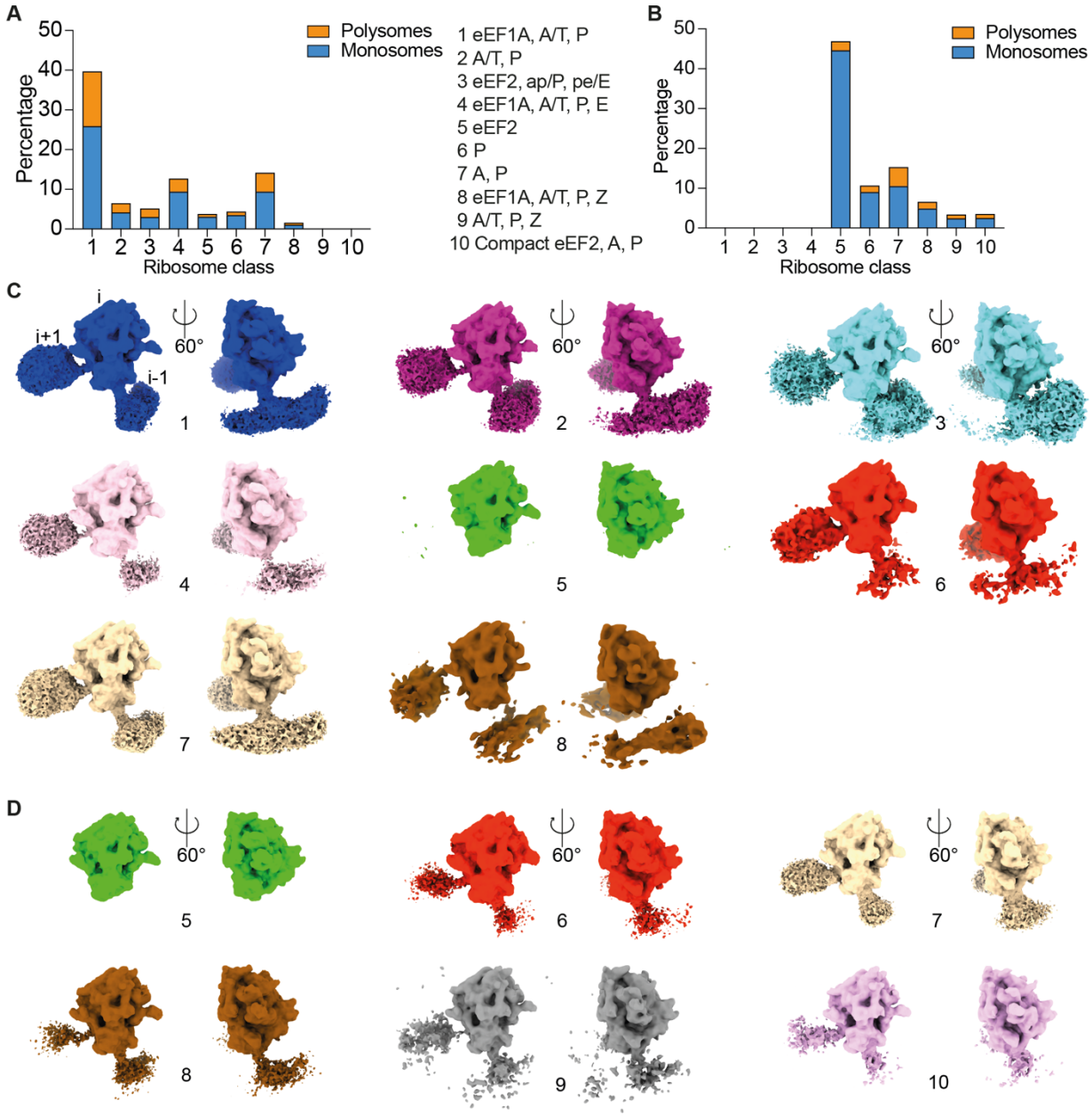

Fig. S16. The neighborhood density of the individual ribosome state.
(**A** and **B**) The abundance of mono-ribosomes and polysomes in each state in untreated cells (A) and HHT-treated cells (B). (**C** and **D**) Gaussian-filtered (sDev = 4) filtered ribosome maps of all detected classes in untreated cells (C) and treated cells (D). The class numbers are shown at the bottom and are same as in (A). i, the leading ribosome. i+1, the potential trailing ribosome.

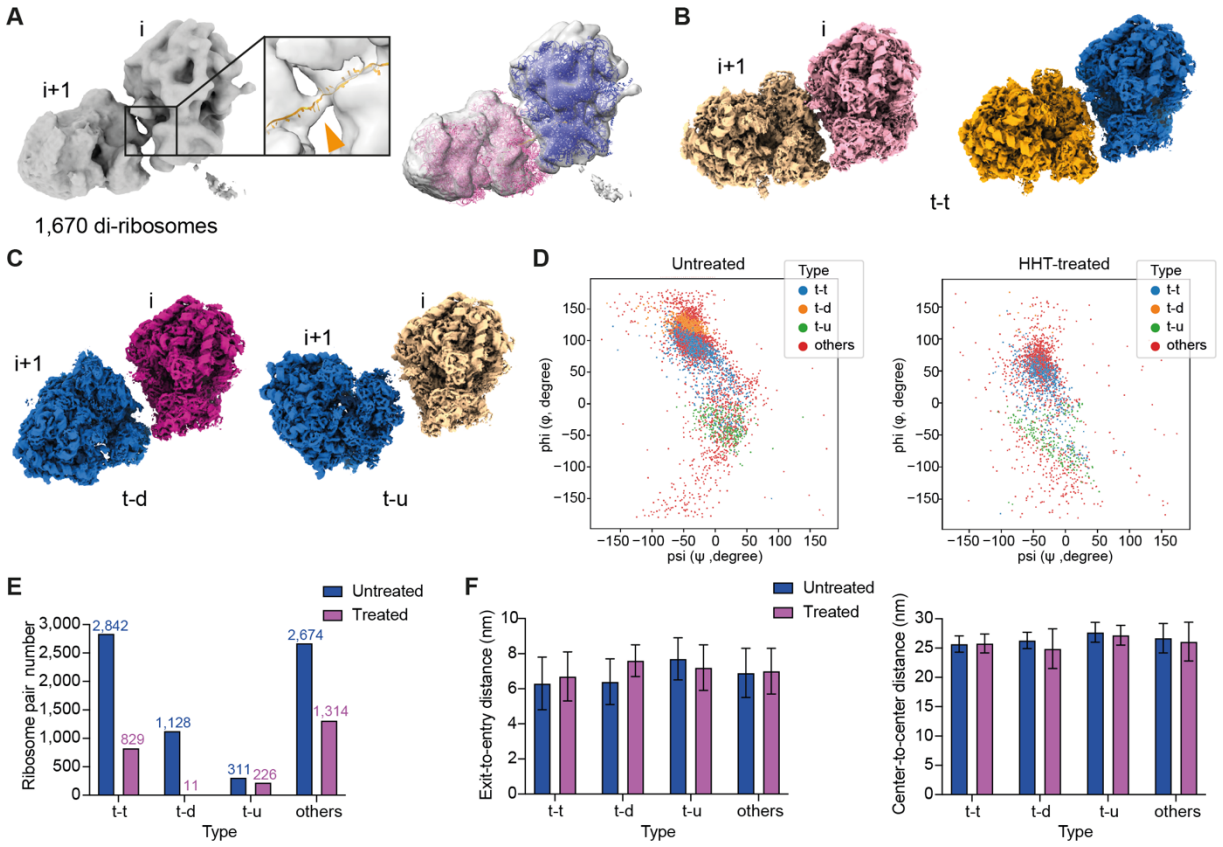

Fig. S17. Analysis of ribosome pairs in polysomes.

(**A**) The subtomogram average map of di-ribosome in untreated cells. The disome model (PDB 6I7O) was rigid-body-fitted into the map. For clarity, only mRNA model is shown in orange (left panel). Triangle, mRNA density. i+1, the trailing ribosome. Human collided disome model (PDB 7QVP) was fitted into the map (right panel). Blue and pink represent the two ribosome structures in the disome model. (**B**) Two representative 't-t' ribosome pairs. The translation states of the ribosome pairs are color coded as in Fig. 4. (**C**) Different preferred assembly of adjacent ribosomes in polysomes. t-d, the central protuberance of the 'i+1' ribosome towards down. t-u, the central protuberance of the 'i+1' ribosome towards up. (**D**) The distribution of t-t, t-d and t-u neighboring pairs within polysomes in untreated (left) and treated cells (right). Ψ and φ of trailing ribosomes' orientations were normalized to the zero rotations of the respective leading ribosomes (Materials and methods). (**E**) The abundance of different configurations of ribosome pairs in polysomes. (**F**) Exit-to-entry distance (left) and center-to-center distance (right) of different types of ribosome pairs in untreated and treated cells. The data represent the mean ± SD. Particle numbers are shown in (E).

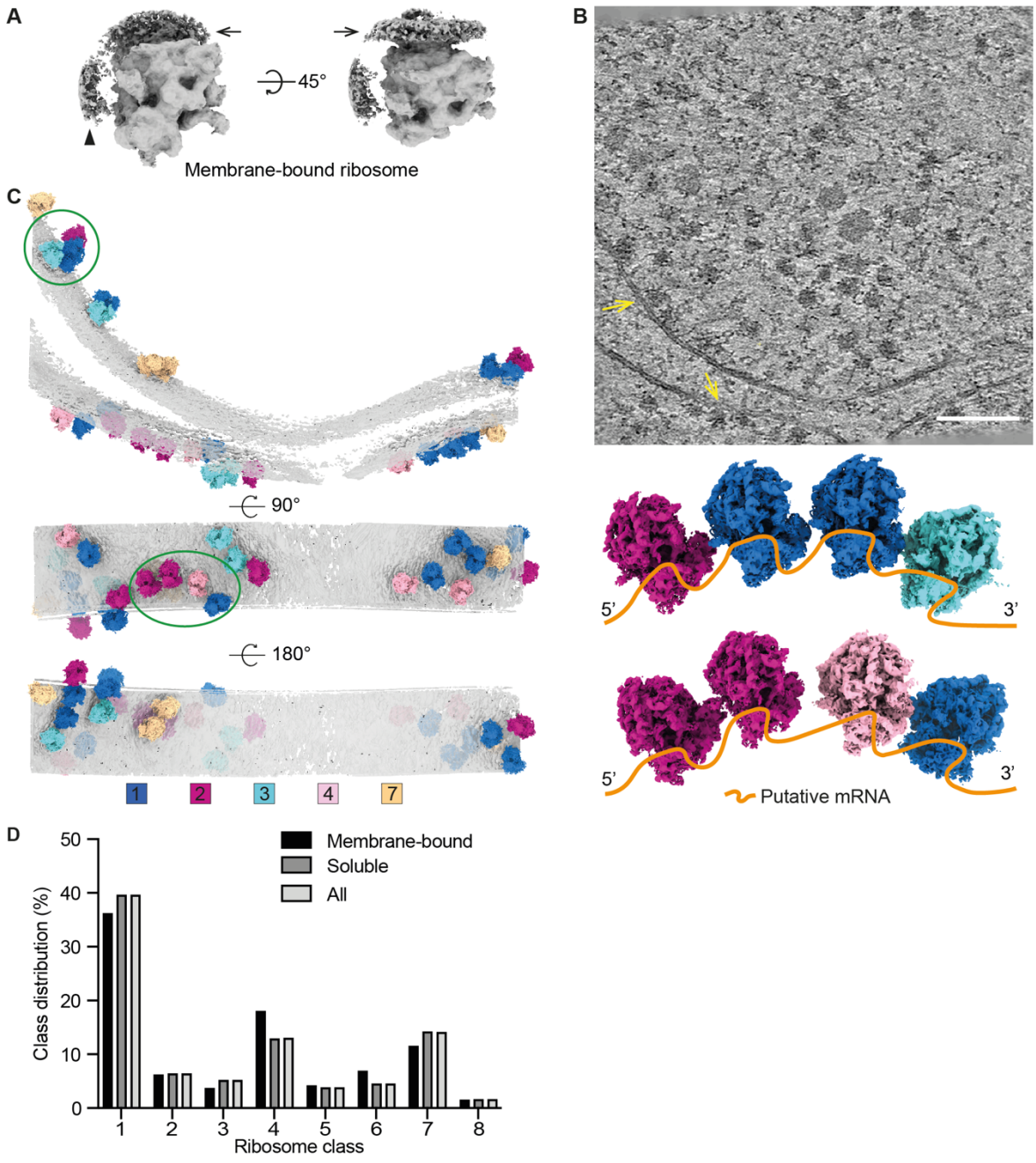

Fig. S18. Membrane-bound ribosomes inside untreated human cells.

(**A**) The sub-tomogram average map of membrane-bound ribosomes in untreated cells. The black triangle shows additional density. Black arrow, membrane. (**B**) A representative tomographic slice shows some ribosomes (yellow arrow) binding on the membrane. Scale bar, 100nm. (**C**) A segmented membrane with ribosomes from the tomogram in (B). The segmented membrane and the translation states are color coded as indicated in the color bar. Two potential membrane-bound polysomes are circled in green (left panel) and reveal the spatial organization and different translation states (right panel). Orange line, putative mRNA. (**D**) The state distribution of membrane-associated and soluble ribosomes (Materials and methods). The classes (1 to 8) are the same as in Fig. 3.

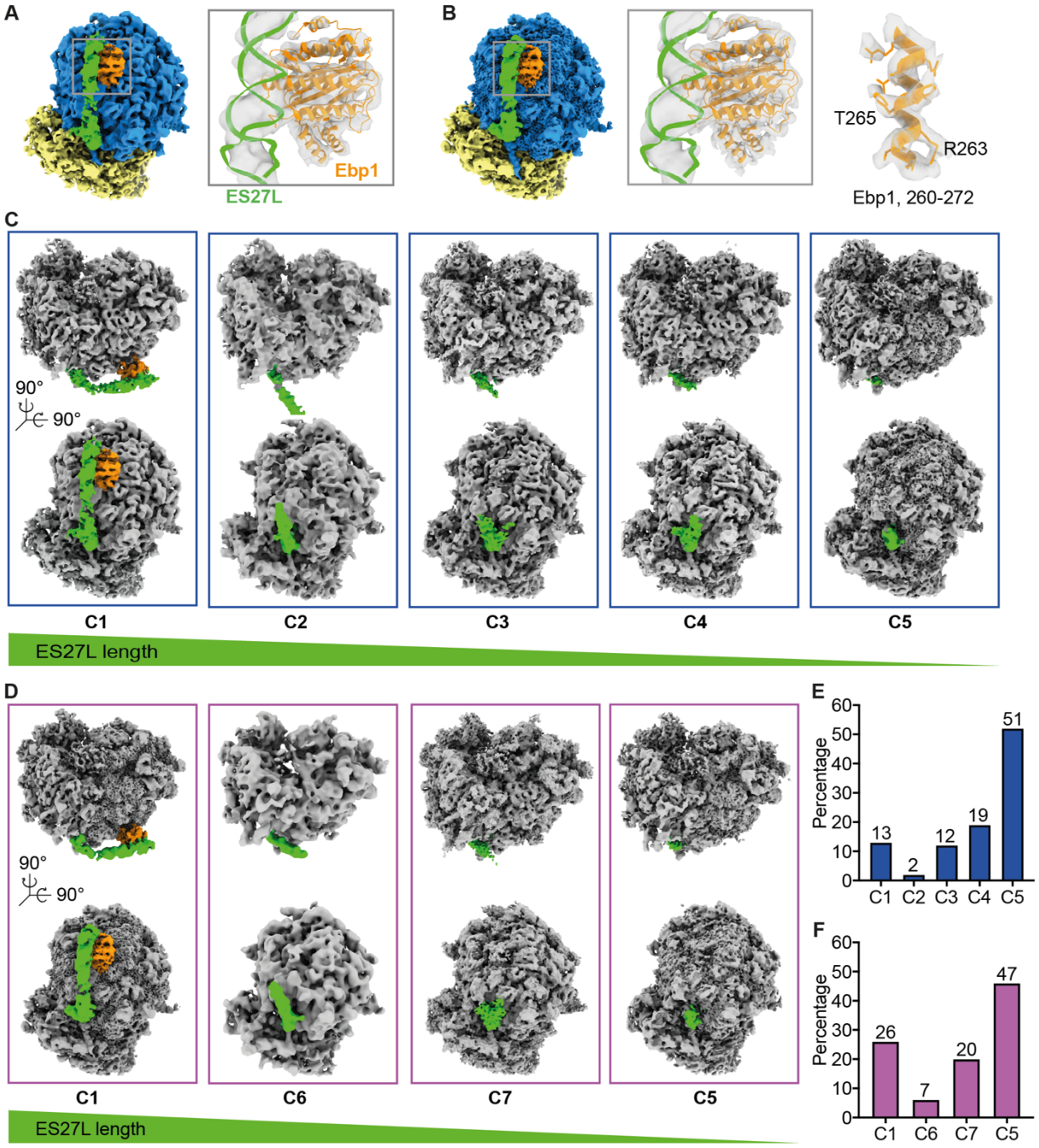

Fig. S19. Structures of ribosome-associated with Ebp1 and ES27L.

(**A** and **B**) Structures of ribosomes bound with Ebp1 from untreated cells (A) and HHT-treated cells (B). PDB 6SXO was fitted into the above maps. (**C**) Different conformations of expansion segment ES27L from the untreated cells. C1 to C5: ribosome conformation 1 to 5. The order of C1 to C5 is defined by the ES27L length. (**D**) Conformations of expansion segment ES27L from the treated dataset. (**E** and **F**) Abundance of C1 to C7 from the two datasets (see tables S2 and S3). Blue, percentage of 39,402 untreated ribosomes. Magenta, percentage of 39,070 treated ribosomes.

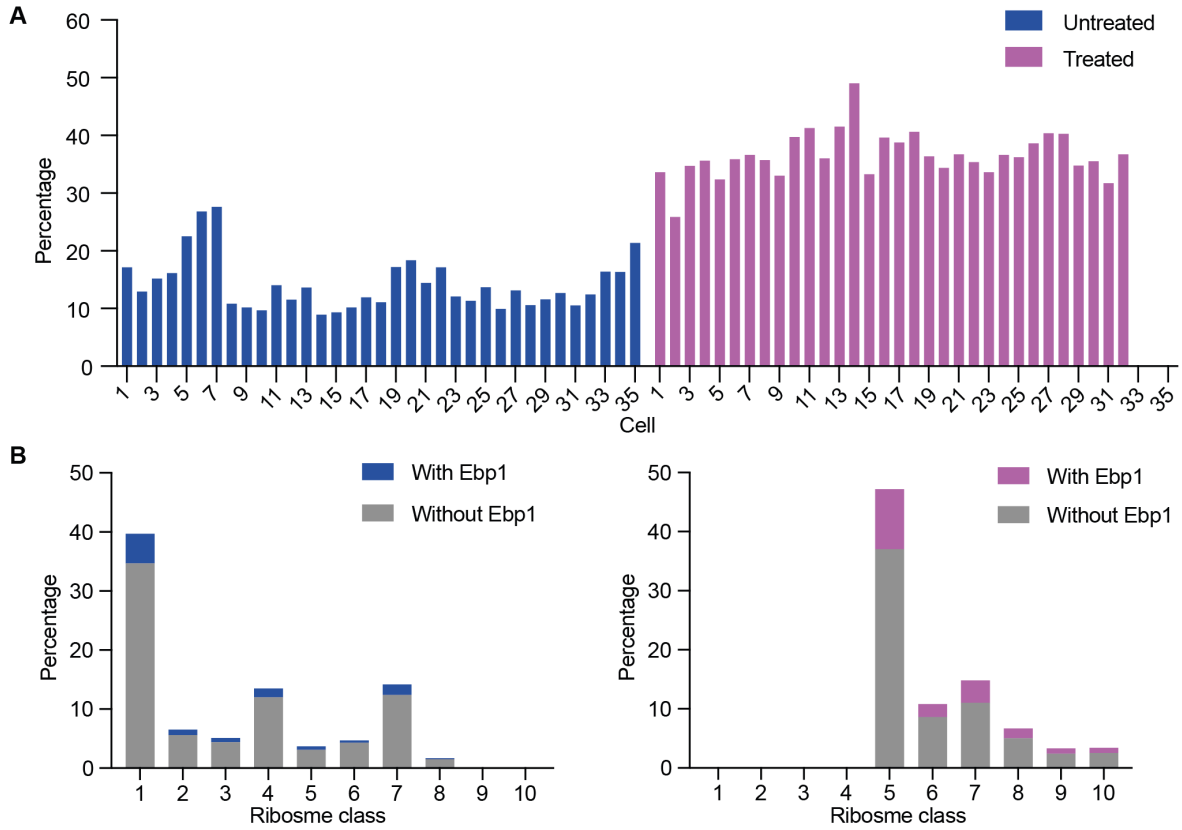

Fig. S20. Translation states and cellular distribution of Ebp1-associated ribosomes. (**A**) Percentage of ribosomes decorated with Ebp1 in 35 untreated and 32 HHT-treated cells. (**B**) Distribution of ribosomes with or without Ebp1 in each ribosome state (the class number is the same as Fig. 3A or fig. S16A). Right, untreated cells. Left, treated cells.

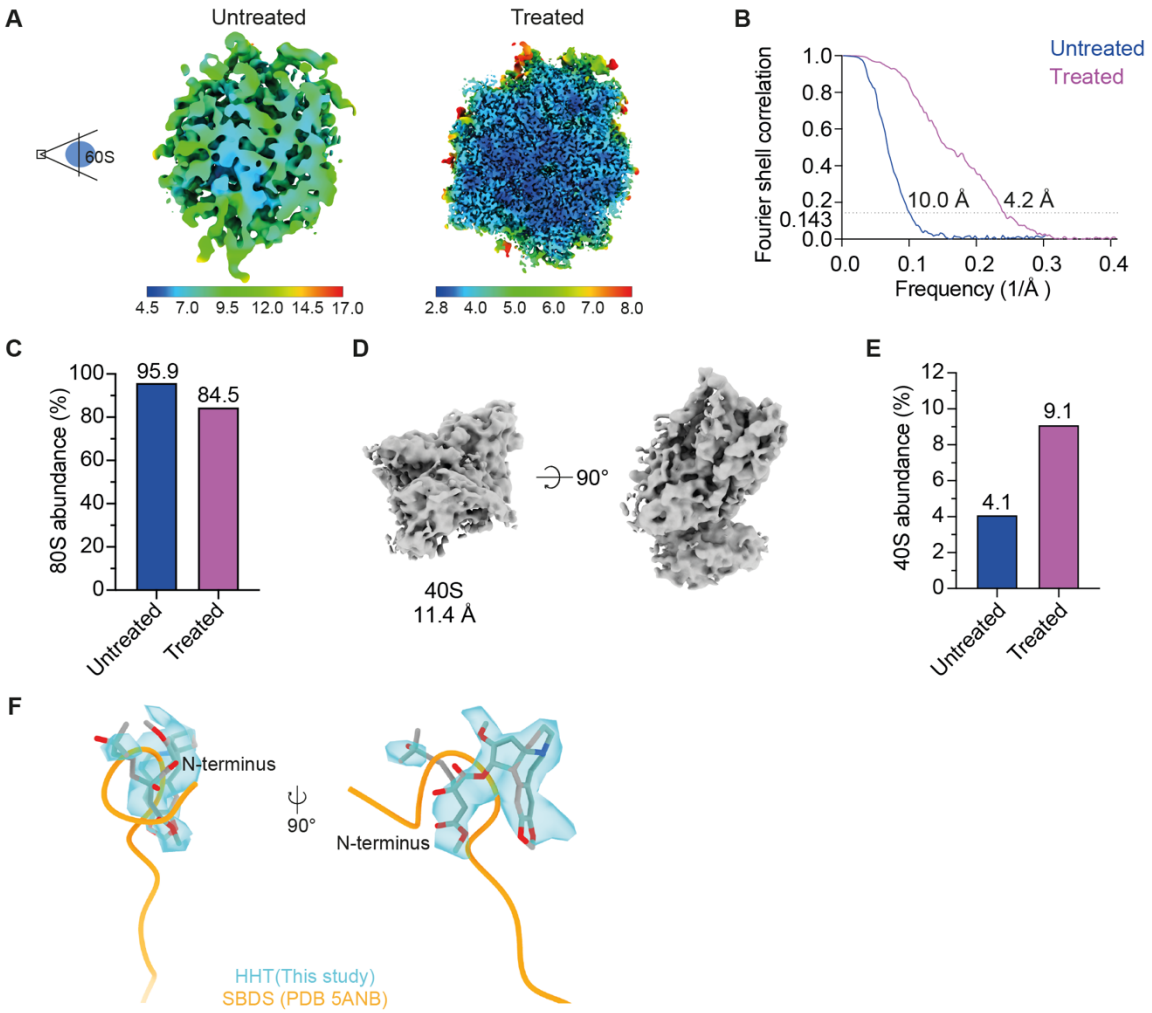

Fig. S21. Structures of 60S and 40S inside human cells.

(**A**) Untreated 60S (left) and treated 60S (right) are colored by local resolution calculated in M. Color keys are shown in the bottom. (**B**) FSC curves of 60S from the two datasets (FSC = 0.143). (**C**) Normalized percentage of the 80S ribosome. Abundance = 80S/(60S+80S). (**D**) Subtomogram average map of free 40S in the cytoplasm of untreated cells. (**E**) Percentage of the 40S in untreated and HHT-treated cells, normalized to the number of 80S ribosomes in the respective dataset. Abundance = 40S/(40S+80S). (F) Atomic model of SBDS-bound 60S (PDB 5ANB) was rigid-body-fitted into our 60S map. Orange, amino terminus (N-terminus) of SBDS. Cyan, HHT density resolved in free 60S in HHT-treated cells fitted with the atomic model from PDB 6QZP.

Table S1. Cryo-EM data collection of the untreated and treated datasets.

	Untreated	HHT-treated
Microscope	Titan Krios G4	Titan Krios G4
Voltage (kV)	300	300
Camera	Falcon4	Falcon4
Magnification	105,000	105,000
Pixel size (Å)	1.188	1.188
Defocus range (μm)	-1.5 to -4.5	-1.5 to -4.5
Automation software	SerialEM	SerialEM
Energy filter slit width (eV)	10	10
Electron exposure (e/Å^2)	120 to 150	120 to 150
Number of tilt series	358	352

Table S2. Cryo-EM data refinement and validation statistics in untreated cells.

	Symmetry imposed	Initial particle number	Final particle number	Resolution (Å) FSC =0.143	Resolution range(Å)	Global B factor (Å^2)
80S ribosome EMD-16721	C1	286,400	39,402	3.2	2.4 to 7.5	-74
80S-eEF1A, A/T, P EMD-16725	C1	286,400	15,587	3.4	2.7 to 8	-48
80S-A/T, P EMD-16726	C1	286,400	2,538	8.3	4.0 to 12	-74
80S-eEF2, ap/P, pe/E EMD-16727	C1	286,400	2,037	9.6	5.1 to 15	-153
80S-eEF1A, A/T, P, E EMD-16728	C1	286,400	5,115	9.4	4.5 to 14	-140
80S-eEF2 EMD-16733	C1	286,400	1,495	11.7	7.7 to 15	-200
80S-P EMD-16734	C1	286,400	1,777	14.7	10 to 20	-200
80S-A, P EMD-16735	C1	286,400	5,574	5.0	3.1 to 8	-77
80S-eEF1A, A/T, P, Z EMD-16736	C1	286,400	636	16.4	9.7 to 20	-200
Di-ribosome EMD-16737	C1	286,400	1,607	18.1	12 to 30	-200
80S ES27L conformation 1 EMD-16738	C1	286,400	5,142	6.6	3.2 to 15	-60
80S ES27L conformation 2 EMD-16739	C1	286,400	832	13.7	10 to 20	-200
80S ES27L conformation 3 EMD-16740	C1	286,400	4,715	6.9	3.5 to 15	-78
80S ES27L conformation 4 EMD-16741	C1	286,400	7,332	4.4	2.9 to 13	-49
80S ES27L conformation 5 EMD-16742	C1	286,400	19,902	3.6	2.8 to 10	-59
Free 60S EMD-16743	C1	286,400	1,693	10.0	4.5 to 17	-178

Table S3. Cryo-EM data refinement and validation statistics in HHT-treated cells.

	Symmetry imposed	Initial particle number	Final particle number	Resolution (Å) FSC =0.143	Resolution range(Å)	Map sharpening B factor ($Å^2$)
80S ribosome EMD-16722	C1	281,600	39,070	3.2	2.4 to 7.5	-69
80S-eEF2 EMD-16744	C1	281,600	18,320	3.7	2.7 to 8	-66
80S-P EMD-16748	C1	281,600	3,990	8.5	4 to 12	-85
80S-A, P EMD-16747	C1	281,600	5,963	4.4	2.8 to 8	-58
80S-eEF1A, A/T, P, Z EMD-16749	C1	281,600	2,607	8.2	3.7 to 12	-91
80S-A/T, P, Z EMD-16750	C1	281,600	1,301	11.5	6.7 to 14	-200
80S-Compact eEF2, A, P EMD-16751	C1	281,600	1,344	11.1	6.3 to 14	-200
80S ES27L conformation 1 EMD-16752	C1	281,600	10,249	4.0	2.8 to 13	-59
80S ES27L conformation 5 EMD-16754	C1	281,600	18,344	3.8	2.8 to 12	-63
80S ES27L conformation 6 EMD-16755	C1	281,600	2,625	11.0	5.8 to 20	-245
80S ES27L conformation 7 EMD-16756	C1	281,600	7,852	4.1	2.9 to 12	-56
Free 60S EMD-16757	C1	281,600	7,176	4.2	2.8 to 8	-45

Table S4. Pseudocode for polysome chain tracing.

Algorithm: Trace polysome chains in a single tomogram

```
untraced_ribosomes = ribosomes
traced_ribosomes = empty list
for each ribosome do
    if ribosome is in untraced_ribosomes then
        trace_chain = true
        current_chain = ribosome
        remove ribosome from untraced_ribosomes
        while trace_chain is true do
            NN = nearest neighbor in untraced_ribosomes
            if the distance to the NN is within the range then
                current_chain = add NN
                remove NN from untraced_ribosomes
            else
                trace_chain = false
                for the first ribosome in current_chain do:
                    NN = nearest neighbor in traced_ribosomes
                    if the distance to the NN is within the range:
                        append current_chain to the existing one
                for the last ribosome in current_chain do:
                    NN = nearest neighbor in traced_ribosomes
                    if the distance to the NN is within the range:
                        prepend current_chain to the existing one
                traced_ribosomes = add current_chain ribosomes
            end if
        end while
    end if
end for
```

Movie S1.
A tomogram and the template matching of 80S ribosomes. For visualization, the tomogram was set to 50% transparency, and the CCC value of 80S was colored in yellow.

Movie S2.
Three-dimensional view of HHT and the neighboring 28S rRNA from the HHT-treated human cells. The atomic model PDB 6QZP was fitted into our map.

Movie S3.
Close view of the Z t-RNA at the 'eEF1A, A/T, P, Z' state in HHT-treated cells. Tangerine, Z-tRNA (PDB 6MTB).